

CONTENTS

1	Introduction	1
1.1	Light Microscopy	2
1.2	Gold Nanoparticles	3
1.3	Luminescence from gold nanoparticles	3
1.4	Applications of gold nanoparticles	4
1.4.1	Tuning the resonance of gold nanoparticles	4
1.4.2	Imaging through detection of anti-Stokes emission	5
1.4.3	Gold nanoparticles as nano-Thermometers	5
2	Cyanide Etching	7
2.1	Introduction	8
2.2	Experimental method.	9
2.3	Results	10
2.4	Conclusions.	15
2.5	Acknowledgements	16
	References	16
3	Background Free Imaging	19
3.1	Introduction	19
3.2	Experimental method.	22
3.3	Results and discussion	24
3.4	Conclusions.	28
3.5	Author Contributions	28
3.6	Acknowledgements	29
	References	29
4	Gold nanoparticles as nano-thermometers	33
4.1	Introduction	33
4.2	Experimental method.	36
4.3	Results	37
4.4	Conclusions.	43
	References	44
A	KCN	49
A.1	Solution Results.	49
A.2	SEM Images.	50
A.3	Background Spectrum	53

B Background Free	55
B.1 Setup	55
B.2 Uv-Vis spectrum	56
B.3 Filters	56
B.4 TEM Images of rods	57
B.5 White light transmission	57
B.6 Full scan without dye	57
B.7 Full scan without dye	59

1

INTRODUCTION

This is the abstract of the introduction

1

1.1. LIGHT MICROSCOPY

MICROSCOPES have become an indispensable tool in all research fields in which there is a need to look at small features. The first microscopes developed by Antoni Van Leeuwenhoek in the XVII century were aimed at studying fabrics; it didn't take long however to discover that nature was hiding amazing elements beyond what the bare human eye could see. The first microscopes focused into developing better lenses and clever illumination schemes.

With the development of the ondulatory theory of light a fundamental limitation for optical microscopes appeared: the diffraction limit. Abbe realized that no matter how good a lens is, there will always be a limit to how much it is possible to focus light. This limit is determined mainly by the wavelength of the employed light beam and by the maximum angle the lens is able to focus.

The diffraction limit puts a restriction to the size of the structures that can be resolved under an optical microscope. The use of shorter wavelengths, as X-Rays opened the possibility to study much smaller structures. However this was at an expense of observing very well defined periodic structures, such as crystals. Soft matter samples such as cells would therefore be out of the scope of these techniques.

It was at the end of the XX century however that a major breakthrough occurred in the field of optics: the detection of a single-molecule fluorescence by M. Orrit and J. Bernard. Single-molecules opened the door to studying materials with unprecedented spatial resolution, but also to determine properties that would have been hidden by bulk broadening. The first studies were done at low temperature (few Kelvins) and allowed to determine properties not only of the fluorescent molecules but also of the hosting matrices, mainly polymers and crystals.

With a growing interest in the field, a big effort was placed in allowing the detection of single-molecules at room temperature. This led to the development of new organic dyes and to establish single-molecule fluorescence microscopy as one of the cornerstones of many research fields. Localization of single fluorophores led to the development of what is now known as super resolution microscopy. By carefully determining the centroid of the emission pattern, it is possible to determine the center a molecule with higher accuracy than what the diffraction limit would allow.

Molecules however show blinking and bleaching. At room temperature it is impossible to prevent fluorophores from going to dark states, meaning that their fluorescence signal will disappear either for a short period of time or for the remaining time of the experiment. This puts a hard limit to the experiments that can be performed employing single-molecules, since they cannot be observed for extended periods of time. Tracking is limited to few seconds, imaging is limited to few frames or to cleverly engineered illumination strategies.

As single-molecule detection allowed to bridge the length mismatch between visible light and biologically relevant scales, new agents that can fill the gap between biologically relevant time scales and fluorophores' observation times are of utmost importance. In this direction different approaches were taken, including employing scattering instead of fluorescence, the use of semiconductor quantum dots and of metallic nanoparticles. The latter are the focus of this thesis and of the next few sections.

1.2. GOLD NANOPARTICLES

Metallic nanoparticles have been subject of studies for a long time. In a fortuitous way Romans managed to generate red-coloured glass by dispersing gold nanospheres into their glass mixing strategies; the beautiful Lycurgus cup is the only surviving example of such technique, together with some other glass fragments of the time. The nanoparticles in the glass preserved their optical properties for centuries, however the explanation of the phenomenon came several centuries later.

Gustav Mie in 1908 calculated the scattering of a plane wave incident on spherical particles. It relies on fully solving Maxwell equations and nowadays it is simply known as Mie scattering. In the original paper it is possible to observe the resonance of gold nanoparticles at around 550 nm; both calculation and measurements show a peak in the scattering efficiency at those wavelengths. Because of the weaker interaction with light of longer wavelengths, the reddish color of colloidal gold nanoparticles can be explained.

Metals however show another interesting property that is given by the oscillation of conduction electrons and is known as plasmon. For particles much smaller than the incident wavelength, a simplification of the Mie formalism can be made by considering only the first order. In this case the polarizability of a nanosphere is given by

$$\alpha_{\text{sphere}} = 3\epsilon_0 V \frac{\epsilon(\omega) - \epsilon_m}{\epsilon(\omega) + 2\epsilon_m} \quad (1.1)$$

where ϵ_0 is the permittivity of vacuum, $\epsilon(\omega)$ is the permittivity of the metal as function of incoming excitation frequency ω and ϵ_m is the permittivity of the surrounding medium. The absorption cross section can thus be calculated as $\sigma_{\text{abs}} = k \text{Im}(\alpha)$ and the scattering as $\sigma_{\text{scatt}} = k^4 |\alpha|^2 / (6\pi)$.

From equation 1.1 it is possible to see that a resonance will appear when $\text{Re}(\epsilon(\omega)) = -2\epsilon_m$. It is important to note that the resonance is therefore dependent not only on the particle's material properties but also on the surrounding medium's optical constants. In the case of elongated nanoparticles, some correction factors can be introduced to the polarizability. However several computer packages exist to calculate with a great precision absorption and extinction cross sections of arbitrary geometries.

A standard procedure to obtain gold nanoparticles is through wet chemical methods. Even in the best of cases there will be a dispersion in shapes that will give rise to inhomogeneous broadening. The differences between nanoparticles can be observed with electron microscope micrographs, but also optically. Slightly different particles will show different resonances and some quantifiable properties as the quantum yield are going to show a great variation of values, associated to intrinsic properties of individual nanoparticles. Moreover, it has been shown in the past that some interesting properties will be concealed in bulk measurements, therefore making single-particle experiments of great importance.

1.3. LUMINESCENCE FROM GOLD NANOPARTICLES

Light emission from gold and copper was observed by Mooradian[?] in 1969. In that work, electron and holes in the metal were excited with visible light and the emission was observed at longer wavelengths. Strikingly, the emission quantum yield (i.e. the number

of emitted photons per absorbed photon) was in the order of 10^{-10} . In subsequent years several studies showed that this low number could be increased with the presence of sharp edges or tips, but still it would be much lower than what is observed for an organic dye, in the order of few percent at least.

When transitioning from bulk gold to nanoparticles, the interaction of light with metal will be highly influenced by the presence of the plasmon resonance. On one hand nanoparticles will have large absorption cross section in specific wavelength regions, as explained in the previous section. On the other hand the emission spectrum will be also concentrated around the plasmon resonance. It is possible to observe that there is a big overlap between the scattering spectra and the emission spectra of gold nanoparticles.

The emission quantum yield of single gold nanoparticles can be several orders of magnitude higher than bulk values partly due to the presence of sharper edges. Typical quantum yield values are in the order of 10^{-6} , several orders of magnitude lower than single organic dye molecules, but the absorption cross section can be in the order of $10^{-2} \mu\text{m}^2$. The combination of both factors makes it possible to use luminescence to detect single gold nanoparticles in a standard fluorescence microscope.

The luminescence of gold nanoparticles can be excited mainly through two different approaches. It is possible to use a short wavelength laser, as a 532 nm to excite interband transitions in gold, as well as the transverse plasmon resonance if working with rods. The emission from the particles can be collected after placing a notch or long pass filter in the detection path to prevent the excitation light to reach the detectors. This allows to collect the entire plasmonic emission.

Another approach to observe the luminescence is to excite the particles close to the resonance. In this way it is possible to exploit the higher absorption cross section but the emission will be mainly concentrated around the excitation wavelength. The presence of detection filters will therefore block a non-negligible part of the spectrum. Both approaches have advantages and disadvantages that will be discussed through the chapter of this thesis.

Gold nanoparticles can therefore be easily compared to single organic dye molecules. Since they emit light at different wavelengths than the excitation wavelength it is possible to achieve a high spectral selectivity when observing them and therefore a relatively high signal-to-background ratio. Applications that require long observation times would therefore highly benefit from the use of metallic nanoparticles that are very stable over time and under a variety of conditions.

1.4. APPLICATIONS OF GOLD NANOPARTICLES

1.4.1. TUNING THE RESONANCE OF GOLD NANOPARTICLES

The previous two sections highlight different strategies for detecting single gold nanoparticles, as nanospheres or nanorods. The principal characteristic of the particles is the presence of a localized surface plasmon resonance. The resonance wavelength (or energy) will be given by the geometry of the particle and by the surrounding medium's properties, as can be the refractive index or temperature. Normally the geometry is determined during the synthesis procedure and thus the resonance is fixed after immobilizing the particles on a substrate.

Chapter 2 focuses into tuning the plasmon resonance *in-situ*, once they are immobilized on a substrate and optically characterized. Currently two approaches exist for tuning the plasmon resonance after synthesis: (1) it is possible to tune the refractive index of the medium using an electric or magnetic field[?]. (2) It is possible to induce shape modifications of the nanoparticles either through chemical[? ? ? ?] or physical means[? ? ?].

In the majority of the reports a blue-shift of the plasmon resonance has been observed. This means that gold nanorods reshape into spheres, or that edges with higher curvature are softened after chemical etching. For physical processes, as thermal reshaping after excitation with a high-intensity laser this can be explained through a rearrangement of surface atoms to energetically more favorable configurations. In the case of chemical etching, previous works have always focused on bulk measurements in suspension. The tips of the particles tend to be more reactive because they are less protected by surfactants.

Chapter 2 shows that through well known chemistry between gold and cyanide ions it is possible to induce a red-shift of the plasmon. This is modelled through an isotropic etching of the particles, obtaining a good agreement between the calculations and the experiments. The main difference with previous works is the absence of a capping agent on the particles' surface. Controllably changing the shape of nanoparticles is of great importance for experiments where a specific resonance is needed.

1.4.2. IMAGING THROUGH DETECTION OF ANTI-STOKES EMISSION

Gold nanoparticles are ideal candidates for labelling of biological samples because they prove to be innocuous to the cell but also because they can be observed for extended periods of time. The big drawback of gold nanoparticles is their low quantum yield. Since the absorption cross section of the particles scales as their volume, detecting smaller particles in presence of background requires a specific approach.

To overcome these difficulties, several techniques have been developed for imaging gold nanoparticles, including two-photon excited luminescence, photothermal heterodyne detection and interferometric detection. Each of these methods is useful but their operation requires dedicated setups and a high level of expertise.

Chapter ?? of this thesis shows that it is possible to image gold nanorods in biologically relevant conditions through detection of the anti-Stokes emission. By placing a short-pass filter in the detection path the background level is reduced significantly, while the luminescence signal from the particles remains high. This is valid even in the presence of cells stained with ATTO647N, a high quantum yield dye. Through conventional Stokes-shifted emission it is not possible to observe any single nanoparticle while the anti-Stokes scheme allows signal-to-background ratios of more than 10.

The technique presented in chapter ?? can be readily implemented in any conventional microscope by the addition of the appropriate filters. It does not require any special operation nor infrastructure. Moreover any data analysis tool for tracking, imaging, centroid extraction, etc. can readily be implemented without further modifications.

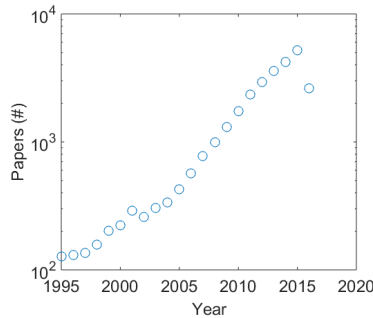


Figure 1.1: Number of papers published containing the terms Plasmonic Photo Thermal Therapy since 1995. Note the logarithmic scale in the y-axis.

1.4.3. GOLD NANOPARTICLES AS NANO-THERMOMETERS

During the past two decades there has been an increasing interest in gold nanoparticles as possible agents for medical treatments. The strong interaction between the particles and light makes them ideal candidates not only for labelling but also for dissipating heat into very localized environments. This simple approach can be used for instance to induce death of cancer cells and is sometimes referred to as Plasmonic Photo Thermal Therapy (PPTT). Figure ?? shows the number of papers published in this field since 1995. The more-than-exponential increase serves as a measure for the relevance this group of techniques is gaining.

After decades of research there is however almost no information regarding the exact temperature that needs to be reached by the nanoparticles to induce cell death. Much less is available at a single-particle/single-cell level. Moreover the field of thermometry at the nanoscale is subject to a moderate debate since some experimental findings contradict expected values from thermodynamic considerations.

Chapter ?? of this thesis focus into the characterization of the mechanisms that give raise to anti-Stokes luminescence. Discarding multi-photon processes, the only way in which is possible to observe a photon with a higher energy than the excitation energy is through interactions with thermal baths. In a nanoparticle electron and holes can interact amongst other things with phonons as summarized section ??.

By carefully fitting the luminescence spectra of single gold nanorods and nanospheres it is possible to compute the surface temperature. The method presented in chapter ?? does not depend on any previous calibration and can be performed in any confocal microscope with a couples spectrometer. The chapter shows the increase in temperature with increasing laser powers and also shows that the luminescence spectra changes when increasing the medium's temperature.

The results from the chapter can have a significant impact on an emerging community that addresses one of the most pressing health issues nowadays.

1.4.4. PLASMON DAMPING AS FUNCTION OF TEMPERATURE

Luminescence is not the only way of detecting gold nanorods with an optical microscope. Gold nanoparticles have a big scattering cross section coinciding with the plas-

mon resonance. If excited with a white light source it is possible to record the scattering spectra without much inconvenience. The shape of the resonance is affected by the surrounding conditions. For instance changes in refractive index of the medium induce changes in the resonance position, while different temperatures of the particles will show different plasmon damping rates.

In principle there are four main mechanisms responsible for the damping of the plasmons: electron-phonon coupling, electron-surface interactions, electron-electron collisions and radiative damping. Out of those only the coupling with phonons shows an appreciable dependence on temperature. Therefore studying the dependence of the plasmon width with temperature can provide another way of measuring temperature.

Chapter ?? focuses on the characterization of the plasmon resonance of single gold nanorods at various temperatures. The plasmon width increases linearly with temperature, as predicted from the Debye model of phonons. Measuring the broadening of the resonance can then be related to changes in temperature of the surrounding medium.

Using the scattering signal benefits from the high cross section of the particles; however the broad distribution of widths and broadening rates found in the studies of chapter ?? does not allow to perform an absolute temperature measurement but to measure a relative change. This is similar to other experiments performed with quantum dots and therefore expand the toolbox of available techniques for thermometry at the nanoscale.



2

***In situ* TUNING OF GOLD NANOROD PLASMON THROUGH OXIDATIVE CYANIDE ETCHING**

Single gold nanorods exhibit great opportunities for bio-sensing, enhanced spectroscopies and photothermal therapy. A key property of these particles is the surface plasmon resonance, that is strongly dependent on their shape. Methods for tuning this resonance after the synthesis of the particles are of great interest for many applications. In this work we show that, through very well known chemistry between gold atoms and cyanide ions, it is possible to tune the surface plasmon of single 25 × 50 nm rods by more than 100 nm towards longer wavelengths. This is achieved by slowly etching gold atoms from the surface of the particles, preserving their specific optical properties.

Parts of this chapter have been published in Physical Chemistry Chemical Physics 18 (23), 15619-15624.[?].

2.1. INTRODUCTION

Gold nanoparticles exhibit large absorption and scattering cross sections with resonances ranging from the visible to the near-infrared. This property is closely related to the surface plasmon, a collective oscillation of conduction electrons that depends on the shape of the particles. For gold nanorods (AuNR) the surface plasmon resonance (SPR) wavelength depends on the aspect ratio (AR) of the particle and can be found between 540 nm for spheres with AR of 1 to beyond 800 nm for elongated particles. The SPR of gold particles can be observed by recording their scattering or luminescence spectrum[1]. Both show a near exact overlap for a large range of wavelengths[2].

The surface plasmon presents great opportunities in (bio-) sensing[3], enhanced spectroscopies [4], photothermal therapy[5] and for concentrating light below the diffraction limit[6]. Success in many of these applications requires precise and *in situ* control over the nanoparticles' plasmon resonance energy. For example, maximum fluorescence[7] or Raman enhancement[8] is achieved when the nanoparticles' plasmon resonance is tuned to the excitation laser wavelength. As another example, efficient photothermal therapy requires the nanoparticles' SPR to be tuned to the near-IR to minimize the damage to healthy cells[9].

Typically the SPR is tuned by carefully manipulating the shapes of nanoparticles during their synthesis. Particularly useful are the rod-shaped particles, whose resonance can be found between 600 nm and beyond 1000 nm, depending on their aspect ratios. Adjusting the concentrations of gold seeds and silver nitrate during the seed-mediated growth[10] is the usual way for producing particles with different resonances. Many other nanoparticle shapes such as nanoprisms, nanorice, nanocubes, nanoshells, etc. have been synthesized with their plasmon resonances covering the entire spectral range from visible to near-IR[11]. Wet-chemical synthesis methods, however, generally yield a broad distribution in nanoparticle sizes and/or shapes, hindering precise and reproducible experiments that need a particular resonance. Furthermore, these methods do not provide any *in situ* adjustment of the SPR, any change of which requires a new synthesis.

For the past decade, single-particle experiments have provided insight into processes that would have been averaged out in bulk experiments. For instance, pump and probe experiments on single particles avoid assumptions regarding size distributions of the sample[12, 13]. Nonlinear processes such as second (or third) harmonic generation can be studied when the particles' plasmon is well characterized and single-particle experiments allow to overcome the inhomogeneous broadening of a sample in suspension[14, 15]. Enhanced spectroscopies normally rely on well defined structures fixed on a substrate[16]. Most of these experiments will benefit from techniques that allow to tune *in situ* the plasmon resonance and geometry of specific particles once they are immobilized on a substrate and optically characterized.

Recently, new methods have been developed to tune nanoparticles' SPR after their synthesis. These approaches can be divided into two broad categories: (1) The first group of methods tune the refractive index of the medium using an electric or magnetic field[17]. The advantage of these methods is that the SPR shift is reproducible and reversible. However the tuning range is rather limited and continuous tuning within this range is difficult to achieve. (2) The other set of approaches rely on controllably inducing

shape modifications of the nanoparticles to tune the plasmon resonance through chemical or physical means. For example, thermal reshaping was induced by illuminating the nanoparticles with an intense, pulsed [18, 19] or continuous laser[2]. Increasing the particles' temperature therefore leads to changes in shape, favoring those conformations with a lower surface energy (i.e. spheres over rods, etc.). Chemical reshaping is also possible and was the focus of several studies[20–24]. In those cases, the capping agent will induce different reactivities on the sides than on the tips of the particles; because of a higher curvature[25] the tips are normally more susceptible to chemical reactions, leading to an anisotropic reshaping shortening the long axis or softening any high-curvature region. Both in the case of laser-induced or chemical-induced reshaping the outcome is usually a blue-shift of the surface resonance peak.

In this work we present a new approach for precise and *in situ* tuning of plasmon resonances of single gold nanorods isolated and immobilized on a glass surface. A nanorod's plasmon resonance is tuned over 130 nm, starting from 650 nm up to 780 nm. Our method exploits well-known chemistry between gold and cyanide ions (CN^-) to controllably etch gold atoms from the nanoparticle and thereby change its aspect ratio. We note that unlike many of the previous studies, here we observe a SPR red shift on gold nanorods. We also verified the results from scanning electron microscopy (SEM) images of the particles and by simulations based on the discrete dipole approximation method. Contrary to previous works where the etching was preferred at the tips, we attribute the red shift to isotropic etching of gold nanorods from all sides resulting in an increase of aspect ratio.

2.2. EXPERIMENTAL METHOD

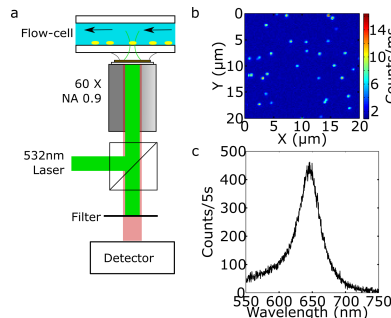


Figure 2.1: Experimental setup and examples of observations. a) Simplified schematic of the confocal microscope employed during the measurements. b) A typical 1-photon luminescence raster scan of the sample immersed in water, before etching and c) luminescence spectrum of a single rod.

Gold nanorods were synthesized by following standard seeded-growth method[26]. The average size of nanorods was $50\text{ nm} \times 25\text{ nm}$ and their SPR is located at 620 nm in water (refer to the Supplementary Information for SEM images and bulk extinction spectra of nanorods as synthesized).

Single-particle measurements were done on a home-built confocal microscope (Figure B.1a). A 532nm laser was used for exciting the particles. The excitation power was $300\text{ }\mu\text{W}$ at the back aperture of the objective (Olympus 60 \times , NA0.9 air). Since the laser

employed is not in resonance with the longitudinal plasmon, the power dissipated by the particles is not high enough as for showing thermal reshaping. After several minutes of irradiation the plasmon position didn't show any shift. Typical powers needed for reshaping are in the range 1 – 5 mW[2]. The luminescence signal was filtered with two 532 nm notch filters and was detected by either an avalanche photodiode or a liquid-nitrogen-cooled CCD-spectrometer (Acton 500i). The images were acquired by scanning the sample across the tightly focused laser beam using a XYZ piezo scanning stage (PI Nano Cube). Figure B.1b shows a typical result from a raster scan. Each bright spot corresponds to a single nanoparticle.

Samples were prepared by spin-casting a suspension of AuNR on clean coverslips. Afterwards the slides were thoroughly rinsed with Milli-Q water and placed in an ozone cleaner for one hour to eliminate any trace of the surfactant (cetyltrimethylammonium bromide, CTAB.) To perform the measurements, the samples were mounted on a flowcell and the initial spectra were taken with the rods immersed in Milli-Q water. Figure B.1c shows an example of the luminescence spectrum of a single particle. Having this initial characterization allowed us to discard clusters of rods[27] from the study.

Of each sample, approximately 10 different particles were selected. Afterwards a solution of KCN was flowed into the sample chamber and spectra of each particle were acquired consecutively after focusing on each one. The time resolution varies according to the exposure time and number of particles studied; in this work a spectrum of each particle was taken at least every minute. Concentrations of KCN ranging from 10 μM to 80 μM were employed with different samples.

2.3. RESULTS

Figure B.1b shows a typical one-photon-excited luminescence image of gold nanorods isolated on a glass surface and covered with water. Single-particle spectra display a narrow Lorentzian lineshape[27] while clusters show additional features or a broad spectrum. Figure B.1c shows a typical spectrum originating from a single nanoparticle. In the samples analyzed more than 90% of the diffraction-limited bright spots originate from single gold nanorods.

Figure 2.2a shows the one-photon luminescence spectra of a gold nanorod immersed in 20 μM KCN at intervals of 70 s. We clearly observe a gradual red shift of the nanorod's plasmon resonance by more than 100 nm over a time interval of 300 s. The left inset of Fig. 2.2a shows the integrated intensity of the particle as a function of time. It is possible to observe a decrease of the intensity by a factor 4 during the same interval in which the shift was observed. Fitting each spectrum with a Lorentzian function allows to extract the resonance wavelength at each recorded time. A more detailed analysis shows that the nanorod's plasmon resonance wavelength varies almost linearly with time as shown in the right inset of Fig. 2.2a.

We note the presence of an additional shoulder peak at 650 nm which is more prominent for the less intense curves. We attribute this shoulder to Raman scattering by the O-H stretching modes of water, between 3000 cm^{-1} and 3600 cm^{-1} . Excitation at 532 nm produces Stokes emission between roughly 630 nm and 650 nm, as observed directly on the background spectrum shown in Figure S3. This Raman band is not completely eliminated upon subtraction of the background spectrum from that of the particle. This non-

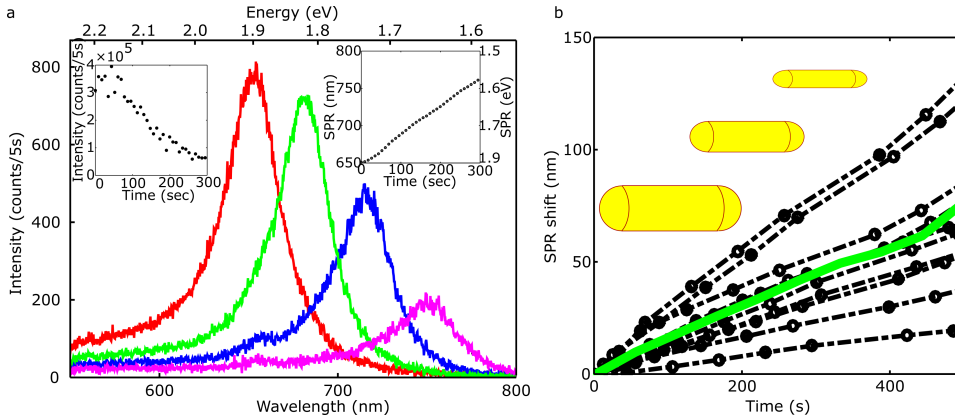
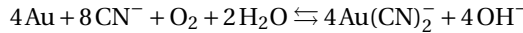


Figure 2.2: One-photon-excited luminescence spectra of gold nanorods immersed in $20\text{ }\mu\text{M}$ KCN. a) Plasmon shift of a single rod. The curves are displayed at 70s intervals. The insets display the integrated intensity of the peak and the resonance wavelength as functions of time, respectively. b) Timetrace of the peak wavelength for 10 different particles immersed in $20\text{ }\mu\text{M}$ KCN. The green solid curve is the average of all the particles.

additivity of the spectra indicates that water Raman scattering is significantly enhanced by the near-field of the nanorod[28].

All the studied nanorods present the same qualitative behavior. Our results are summarized in Fig. 2.2b, which shows the shift of plasmon resonance wavelength as a function of time for ten different rods (dashed lines). Each nanorod shows a red shift of the plasmon resonance wavelength which varies almost linearly with time irrespective of the initial resonance wavelength. The rate of SPR shift, however, varies significantly from particle to particle. The highest observed rate was 15 nm/minute while the lowest one was 2 nm/minute. The green curve in Figure 2.2b is the average of all the shifts; since spectra of each particle were acquired sequentially, we interpolated the values of the shift at intermediate times to compute the average.

The reaction between gold and potassium cyanide is well known and is used for gold mining, electroplating, etc. Gold reacts with aqueous CN^- ions in presence of oxygen to form $\text{Au}(\text{CN})_2^-$, which is soluble in water. The reaction can be written as follows



In our experiment the formation of $\text{Au}(\text{CN})_2^-$ results in gold etching from the nanorods, as has been reported previously[22].

The etching of gold atoms from a nanorod has two effects: Firstly, the nanorods' volume will decrease gradually with reaction time. This is consistent with our observation that the one-photon-excited luminescence intensity decreases with time. Secondly, the aspect ratio of a nanorod can either decrease or increase depending on the preferred direction of etching. The Nanorod aspect ratio will decrease with time if the reaction happens preferably at the tips. This is indeed the case for nanorods protected with CTAB and dispersed in solution[22]. CTAB binds more weakly to the tips than to the sides and therefore leaves the tips more susceptible for chemical reactions[29]. The consequent

decrease of aspect ratio yields a blue shift of the plasmon resonance[30]. If etching happens isotropically from both sides and tips, an overall increase of the nanorod's aspect ratio results, as is depicted schematically in Fig. 2.2b. This is the more likely scenario in our experiment as the nanorods' surface does not have any protective CTAB bilayer.

2

Numerical simulations based on the discrete dipole approximation were performed to assess the hypothesis that the red shift of the plasmon resonance is due to isotropic nanorod etching. The initial dimensions of the particles were fixed at $25\text{ nm} \times 50\text{ nm}$ which coincide with the median values of the distribution of sizes of our nanoparticles (see SI). Simulations are carried out in etching steps of 0.5 nm . Figure 2.3a shows the calculated scattering spectra of the particle at different etching steps. We clearly observe a red-shift of the plasmon resonance wavelength, in concordance with what was observed in our experiment. The first inset of the figure shows the decrease of the maximum scattering cross section spectrum as a function of etched thickness.

Comparing experimental and simulated data can be achieved by fixing the value of the etching rate. In our case the best approximation to the particle shown in Figure 2.2a is achieved by setting the etching rate to 1 nm/min . Comparison to simulations for different nanorods would in principle allow us to check the consistency of the assumption of a constant etching rate for all rods. Indeed, both volume and aspect ratio of the rod can be determined by comparison of experimental data to simulations. A new comparison after a given etching time would give the changes in volume and aspect ratio, which should be consistent with the same etching rate for all rods. In the present work, however, we did not attempt this analysis. We simply used the relative volume as a scaling factor to compare simulations and experiments, as is shown in the right inset of Figure 2.3a.

The luminescence intensity of gold nanorods is roughly proportional to their volume. It is possible therefore to calculate the relative volume of a particle by comparing the total luminescence intensity at a given instant and at a reference time. We employed the initial intensity as the reference, therefore the SPR shift increases while the relative volume decreases as depicted by the arrow in the inset of Figure 2.3a. The volume of the simulated particle can be directly computed from the geometrical parameters. The inset shows a remarkable agreement between the simulations and the experimental data. For smaller relative volumes (less than 0.1) the recorded spectra is 10 times less intense than the initial one, giving rise to a less accurate positioning of the resonance peak.

Figure 2.3b shows simulated plasmon shift rates for three different series of nanorods. In each series particles have the same initial volume, but different initial plasmon resonance, spanning from 600 nm to 780 nm . The first series corresponds to 5 particles with a volume of 6800 nm^3 (red), the second to 7 particles of 20000 nm^3 (green) and the third to 6 of 25000 nm^3 (blue). The shift rate is defined as the plasmon shift given by etching a thickness of 0.5 nm away from the particle. It can be observed that for larger particles the shift is slower than for smaller ones at the same initial resonance. On the other hand it is also possible to observe that red-shifted particles present a larger shift rate.

The results in Fig. 2.3b are easier to understand considering that the plasmon resonance is closely related to the aspect ratio of the particles (length divided by diameter). Small particles will exhibit a bigger change in aspect ratio when subjected to the same amount of etching than bigger particles. This explains why smaller particles

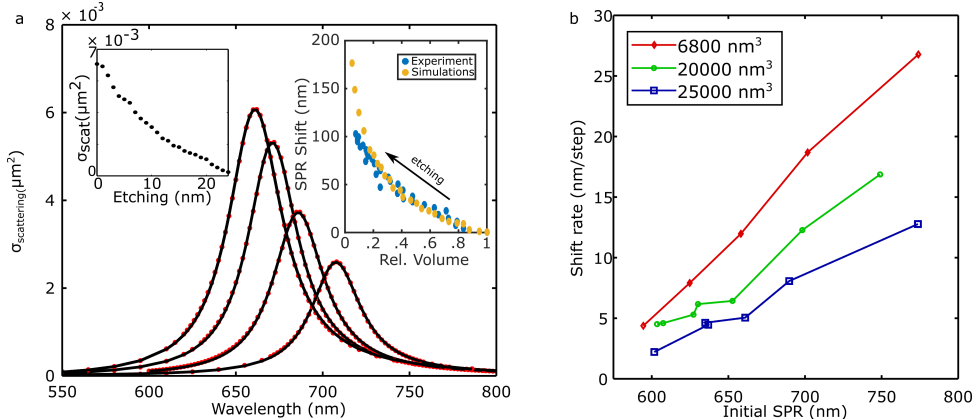


Figure 2.3: Simulated plasmon spectra at different etching stages. a) Examples of the curves obtained at different simulations steps. The black curves are fits with Lorentzians. The left inset shows the maximum scattering cross section as function of etching. The right inset displays the plasmon shift of experimental and simulated data as the relative volume of the particle diminishes. b) Shift rate as a function of the initial plasmon resonance for different particles. The lines correspond to particles with the same initial volume but different initial aspect ratios. As expected from an isotropic etching, larger particles will present a slower plasmon shift and more elongated particles will have a faster one.

show a higher shift rate than more massive ones. On the other hand, volume is not the only factor to take into account. Particles with a higher initial aspect ratio (longer resonance wavelength) will show a faster change in aspect ratio when subjected to the same amount of etching. The interplay between both volume and initial aspect ratio can account for the big variability observed experimentally. This is also supported by the distribution of particle sizes and aspect ratios observed in the SEM images (see SI.)

Figure 2.4a shows the measured FWHM of the plasmon peak for several nanorods immersed in $20 \mu\text{M}$ KCN as a function of the resonance shift. Note that the plot shows the width of the resonance in units of energy and not in units of wavelength. Because of the nonlinear relation between them, the peak width expressed in wavelength depends on the peak position rendering difficult the comparison of widths during the shift. At the beginning of the reaction there is a decrease of the width. Then it stabilizes for shifts between 75 nm and 100 nm. After this point, as the volume of the particles is largely reduced, it is no longer possible to reliably extract information from the spectra. The inset of Fig. 2.4a shows the FWHM obtained from the simulations for a $25 \text{ nm} \times 50 \text{ nm}$ nanorod. The simulated spectrum is slightly narrower than the measured one but the trends are similar.

The initial decrease of the resonance FWHM observed in the experiments may be due to the elimination of defects from the surface of the particles. However, the simulated width that doesn't take into account any surface impurities shows a similar decrease. This behavior can be explained by the decrease of both the radiative and non-radiative damping mechanisms during the etching process. The radiation damping scales as the volume of the particle[31] and therefore will decrease while the cyanide etches gold atoms from the particle. On the other hand we observe that the energy distance be-

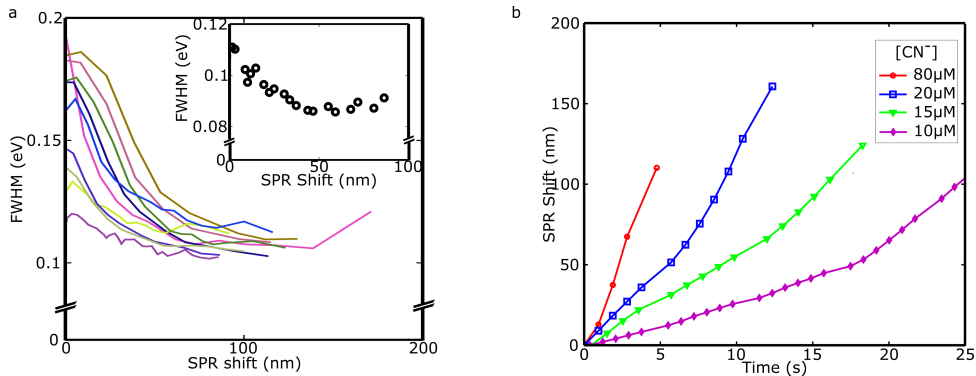


Figure 2.4: a) Measured plasmon FWHM of different particles immersed in 20 μM KCN as a function of their plasmon shift. The inset shows the results from simulations carried out with the ADDA package. b) SPR Shift as a function of time for particles with the same initial SPR at different KCN concentrations.

tween the longitudinal plasmon peak and interband transitions in gold increases during the etching process. Therefore the non-radiative damping mechanisms in the particle may also become less efficient[1]. Both effects combined can account for the diminishing plasmon width that is observed.

Figure 2.4b shows the plasmon peak shift as a function of time for various KCN concentrations for particles with a plasmon peak at roughly 630 nm. As shown for the simulations (Figure 2.3b), the etching rate depends on the initial SPR, therefore it is important to choose particles that are similar to each other. The time-traces of the peak position clearly show that the shift rate is proportional to the concentration of KCN. For every concentration a shift of at least 100 nm was observed. It is important to note that the behavior of the FWHM in all the cases is similar and it resembles the results shown in Figure 2.4a.

Samples of the same nanorods were prepared for scanning electron microscopy (SEM) imaging by drop-casting the same solution of rods. SEM images were acquired before the etching, after 2 min immersion in KCN and after 4 min. In each case we observed that when particles are isolated from each other, the rod shape is preserved. In aggregates of particles this no longer holds and rods start to lose their shape (see Supporting Information for SEM images.) Calculating the distribution of sizes of the particles shows a slight increase in the aspect ratio but this shift is smaller than the width of the distribution.

The simulations also allow us to estimate the volume of gold etched away from a particle by unit of time. For a typical case as the one depicted in Figure 2.4b it is possible to obtain an etching rate of 0.5 nm/min for the 10 μM timetrace. Assuming an atomic radius of gold of 144 pm[32] we obtain that the reaction rate can be as low as 700 atoms per second. From the simulations and these estimates it is possible to approximate the plasmon shift for every etched atom. In the same conditions as before, it would be $0.2 \cdot 10^{-3}$ nm/atom, several orders of magnitude smaller than the sensitivity of our experiments.

The same experiments performed in solution (see SI) show a different behavior of the plasmon resonance. As reported by other groups [22, 25] the rods reshape into spheres.

The presence of CTAB can explain this trend: the tips will be more exposed and therefore react more quickly, yielding a net decrease in aspect ratio. In our single-particle experiments CTAB was removed both by rinsing the samples with water and by placing them in an ozone cleaner. However, the glass surface supporting the rods has to be taken into account. In principle there is a side of the rods in contact with the surface that will be less, or not, exposed to KCN. Etching in this case wouldn't be isotropic and would flatten the rods. Neither the optical nor the SEM images allowed us to assess this question because there is no information on the axis perpendicular to the surface. The deviation of the experiments from the simulations for the smaller volumes may be also dependent on this.

2.4. CONCLUSIONS

In this work we have shown a simple method that allowed us to tune the plasmon peak position of single gold nanorods with nanometer accuracy and over the range of 100 nm (300 meV). More importantly, we show that during the etching process the rod-like shape is preserved; this was confirmed both by monitoring the FWHM of the resonance peak and by acquiring SEM images after different reaction times. The experiments allowed us to record the plasmon peak with a relatively high temporal and spectral accuracy, allowing us to stop the reaction when the resonance is at the desired value.

Discrete dipole simulations with an isotropic etching model allowed us to estimate the amount of gold etched from the nanoparticles. The calculations were consistent with the red-shift of the plasmon and the diminishing intensity of the luminescence signal. The general trend of the FWHM is also correctly reproduced, but the obtained values are slightly different. SEM images of the rods confirmed the values obtained from the simulations. Combining these results provides a way of predicting the behaviour of the plasmon peak for different rods.

We observed a broad distribution of the rate at which the plasmon peak shifts for different particles under the same experimental conditions. This can be attributed to the initial differences in aspect ratios and volumes of each particle. Sphere-like particles will show a small shift since the aspect ratio remains constant under isotropic etching. More elongated particles, on the other hand, will have a much steeper increase in aspect ratio while being etched. Intrinsic differences between particles can also be present, producing different shift rates even if particles have the same plasmon resonance. For instance the faceting of the surface or the presence of left-over CTAB that was not completely washed away or oxidized can induce a slightly anisotropic etching. These differences between particles are impossible to assess by optical means and would require a much more sensitive approach.

The role of the capping agent has largely been studied and has always been held responsible for the observations both in chemical etching[25] and for photothermal reshaping[19]. Avoiding the presence of the passivating layers is impossible in suspension, since gold nanoparticles would aggregate. Our results provide evidence that supports previous observations regarding the effect of the curvature and the accessibility of KCN to the surface of the particle.

2.5. ACKNOWLEDGEMENTS

SK acknowledges financial support from IIT-Gandhinagar. This work is part of the research programme of the Foundation for Fundamental Research on Matter (FOM), which is part of the Netherlands Organisation for Scientific Research (NWO).

REFERENCES

- [1] C. Sönnichsen, T. Franzl, T. Wilk, G. von Plessen, J. Feldmann, O. Wilson, and P. Mulvaney, *Drastic reduction of plasmon damping in gold nanorods*. Phys. Rev. Lett. **88**, 077402 (2002).
- [2] M. Yorulmaz, S. Khatua, P. Zijlstra, A. Gaiduk, and M. Orrit, *Luminescence quantum yield of single gold nanorods*. Nano Lett. **12**, 4385 (2012).
- [3] P. Zijlstra, P. M. R. Paulo, and M. Orrit, *Optical detection of single non-absorbing molecules using the surface plasmon resonance of a gold nanorod*. Nat. Nanotechnol. **7**, 379 (2012).
- [4] S. T. Sivapalan, B. M. Devetter, T. K. Yang, T. van Dijk, M. V. Schulmerich, P. S. Carney, R. Bhargava, and C. J. Murphy, *Off-resonance surface-enhanced Raman spectroscopy from gold nanorod suspensions as a function of aspect ratio: not what we thought*. ACS Nano **7**, 2099 (2013).
- [5] T. Zhao, K. Yu, L. Li, T. Zhang, Z. Guan, N. Gao, P. Yuan, S. Li, S. Q. Yao, Q.-H. Xu, and G. Q. Xu, *Gold nanorod enhanced two-photon excitation fluorescence of photosensitizers for two-photon imaging and photodynamic therapy*. ACS Appl. Mater. Interfaces **6**, 2700 (2014).
- [6] P. Zijlstra and M. Orrit, *Single metal nanoparticles: optical detection, spectroscopy and applications*, Reports Prog. Phys. **74**, 106401 (2011).
- [7] S. Khatua, P. M. R. Paulo, H. Yuan, A. Gupta, P. Zijlstra, and M. Orrit, *Resonant plasmonic enhancement of single-molecule fluorescence by individual gold nanorods*. ACS Nano **8**, 4440 (2014).
- [8] A. D. McFarland, M. a. Young, J. a. Dieringer, and R. P. Van Duyne, *Wavelength-scanned surface-enhanced Raman excitation spectroscopy*. J. Phys. Chem. B **109**, 11279 (2005).
- [9] A. M. Alkilany, L. B. Thompson, S. P. Boulos, P. N. Sisco, and C. J. Murphy, *Gold nanorods: Their potential for photothermal therapeutics and drug delivery, tempered by the complexity of their biological interactions*, Adv. Drug Deliv. Rev. **64**, 190 (2012).
- [10] L. Vigderman, B. P. Khanal, and E. R. Zubarev, *Functional gold nanorods: Synthesis, self-assembly, and sensing applications*, Adv. Mater. **24**, 4811 (2012).
- [11] S. Lal, S. Link, and N. J. Halas, *Nano-optics from sensing to waveguiding*, Nat. Photonics **1**, 641 (2007).

- [12] G. V. Hartland, *Coherent Excitation of Vibrational Modes in Metallic Nanoparticles*, Annu. Rev. Phys. Chem. **57**, 403 (2006).
- [13] P. V. Ruijgrok, P. Zijlstra, A. L. Tchebotareva, and M. Orrit, *Damping of acoustic vibrations of single gold nanoparticles optically trapped in water*. Nano Lett. **12**, 1063 (2012).
- [14] J. Butet, J. Duboisset, G. Bachelier, I. Russier-Antoine, E. Benichou, C. Jonin, and P. F. Brevet, *Optical second harmonic generation of single metallic nanoparticles embedded in a homogeneous medium*, Nano Lett. **10**, 1717 (2010).
- [15] M. Lippitz, M. A. Van Dijk, and M. Orrit, *Third-harmonic generation from single gold nanoparticles*, Nano Lett. **5**, 799 (2005).
- [16] P. Olk, J. Renger, M. T. Wenzel, and L. M. Eng, *Distance dependent spectral tuning of two coupled metal nanoparticles*, Nano Lett. **8**, 1174 (2008).
- [17] P. A. Kossyrev, A. Yin, S. G. Cloutier, D. a. Cardimona, D. Huang, P. M. Alsing, and J. M. Xu, *Electric field tuning of plasmonic response of nanodot array in liquid crystal matrix*, Nano Lett. **5**, 1978 (2005).
- [18] S. Link, C. Burda, B. Nikoobakht, and M. A. El-Sayed, *Laser-Induced Shape Changes of Colloidal Gold Nanorods Using Femtosecond and Nanosecond Laser Pulses*, J. Phys. Chem. B **104**, 6152 (2000).
- [19] Y. Horiguchi, K. Honda, Y. Kato, N. Nakashima, and Y. Niidome, *Photothermal reshaping of gold nanorods depends on the passivating layers of the nanorod surfaces*, Langmuir **24**, 12026 (2008).
- [20] E. Carbó-Argibay, B. Rodríguez-González, J. Pacifico, I. Pastoriza-Santos, J. Pérez-Juste, and L. Liz-Marzán, *Chemical Sharpening of Gold Nanorods: The Rod-to-Octahedron Transition*, Angew. Chemie **119**, 9141 (2007).
- [21] J. Rodríguez-Fernández, J. Pérez-Juste, P. Mulvaney, and L. M. Liz-Marzán, *Spatially-directed oxidation of gold nanoparticles by Au(III)-CTAB complexes*. J. Phys. Chem. B **109**, 14257 (2005).
- [22] N. R. Jana, L. Gearheart, S. O. Obare, and C. J. Murphy, *Anisotropic Chemical Reactivity of Gold Spheroids and Nanorods*, Langmuir **18**, 922 (2002).
- [23] C. K. Tsung, X. Kou, Q. Shi, J. Zhang, M. H. Yeung, J. Wang, and G. D. Stucky, *Selective shortening of single-crystalline gold nanorods by mild oxidation*, J. Am. Chem. Soc. **128**, 5352 (2006).
- [24] W. Ni, X. Kou, Z. Yang, and J. Wang, *Tailoring longitudinal surface plasmon wavelengths, scattering and absorption cross sections of gold nanorods*, ACS Nano **2**, 677 (2008).

- 2
- [25] H. Yuan, K. P. F. Janssen, T. Franklin, G. Lu, L. Su, X. Gu, H. Uji-i, M. B. J. Roeffaers, and J. Hofkens, *Reshaping anisotropic gold nanoparticles through oxidative etching: the role of the surfactant and nanoparticle surface curvature*, RSC Adv. **5**, 6829 (2015).
 - [26] B. Nikoobakht and M. A. El-Sayed, *Preparation and Growth Mechanism of Gold Nanorods (NRs) Using Seed-Mediated Growth Method*, Chem. Mater. **15**, 1957 (2003).
 - [27] A. M. Funston, C. Novo, T. J. Davis, and P. Mulvaney, *Plasmon coupling of gold nanorods at short distances and in different geometries*, Nano Lett. **9**, 1651 (2009).
 - [28] J. B. Snow, S. X. Qian, and R. K. Chang, *Stimulated Raman scattering from individual water and ethanol droplets at morphology-dependent resonances*. Opt. Lett. **10**, 37 (1985).
 - [29] K. K. Caswell, J. N. Wilson, U. H. F. Bunz, and C. J. Murphy, *Preferential end-to-end assembly of gold nanorods by biotin-streptavidin connectors*, J. Am. Chem. Soc. **125**, 13914 (2003).
 - [30] S. Link, M. B. Mohamed, and M. a. El-Sayed, *Simulation of the optical absorption spectra of gold nanorods as a function of their aspect ratio and the effect of the medium dielectric constant*, J. Phys. Chem. B **103**, 3073 (1999).
 - [31] a. Wokaun, J. P. Gordon, and P. F. Liao, *Radiation damping in surface-enhanced Raman scattering*, Phys. Rev. Lett. **48**, 957 (1982).
 - [32] L. Pauling, *Atomic Radii and Interatomic Distances in Metals*, J. Am. Chem. Soc. **69**, 542 (1947).

3

BACKGROUND-FREE IMAGING OF GOLD NANORODS THROUGH DETECTION OF ANTI-STOKES EMISSION

Metallic nanoparticles have opened the possibility of imaging, tracking and manipulating biological samples without time limitations. Their low photoluminescence quantum yield however, makes them hard to detect under high background conditions. In this study we show that it is possible to image gold nanorods by detecting their anti-Stokes emission under resonant excitation. We show that even in a cell containing the fluorescent dye ATTO647N, the signal-to-background ratio of the anti-Stokes emission is higher than 10, while it is impossible to image the particles with the Stokes emission. The main advantage of this technique is that it does not require any major change in existing fluorescence imaging setups, only the addition of an appropriate short-pass filter in the detection path.

3.1. INTRODUCTION

High-resolution microscopy has become an indispensable tool for studying biological samples both in vitro and in vivo[1]. Fluorescent organic dyes are commonly employed to such ends because of their reduced size and high quantum yield[2]. Fluorophores, however, have an inherent constraint in the possible observation time, since molecules eventually bleach under intense illumination[3]. Even the most photostable dyes cannot be imaged at saturation for longer than few tens of seconds. Gold nanoparticles on the other hand are almost indefinitely stable[4] and open up many original applications including photothermal therapy[5] and imaging[6].

As gold nanoparticles do not blink nor bleach[7] [8], they are ideal candidates for labelling[9], tracking[10] and manipulating[11] biological samples over extended peri-

ods of time. Moreover it has been shown that with the proper size and coating, they do not interfere with cells' functioning[12], allowing not only *in vitro* but also *in vivo* studies. Compared to organic dyes, gold nanoparticles are much larger and their emission quantum yield is much smaller, in the order of 10^{-6} [13]. This minute value is compensated by an absorption cross section several orders of magnitude larger than that of molecules[14], therefore the brightness of gold nanoparticles is comparable to that of fluorescent molecules under the same illumination intensity.

3

Since the absorption cross section of the particles scales as their volume, detecting smaller particles in presence of background requires a specific approach. Several techniques have been proposed, including two-photon excitation[6], photothermal heterodyne detection[15] and interferometric detection[16]. Each of these methods are useful but their operation requires dedicated setups and a high level of expertise. A method that allows to image gold nanoparticles with a high background rejection and that is readily implementable in current confocal and wide-field microscopes would provide great benefits.

Gold nanoparticles exhibit a collective oscillation of conduction electrons called surface plasmon resonance[17]. This resonance strongly depends on the shape of the particles[18][19]. Spheres with radius roughly between 5 and 80 nm will have a resonance between 520 nm and 560 nm; more elongated particles such as nano-rods or bipyramids[20] exhibit red-shifted longitudinal resonances that reach wavelengths of 800 nm or longer[21]. It is important to note that tuning the shape of the particles can be easily achieved by synthesis and that relatively narrow size distributions can be obtained[22].

The plasmon is responsible for enhanced absorption and scattering cross sections[23] of particles for specific wavelengths but it is also responsible for enhanced photoluminescence emission in the spectral region of the plasmon resonance. Because of the absence of a gap in the excited states spectrum of gold nanoparticles, their photoluminescence excitation spectra overlaps their emission spectrum[13], a very different situation from the Stokes-shifted emission of fluorescent molecules and semiconductor nanocrystals. Upon excitation of gold nanoparticles at their plasmon resonance maximum, most of the emission will be concentrated in a narrow spectral region around the excitation. This implies that most of the luminescence will be blocked by the filters that, in fluorescence detection experiments, prevent direct excitation light from reaching the detectors.

It is also possible to excite the particles off-resonance with a shorter wavelength laser (for instance through interband transitions with 532 nm) and the emission will be mostly concentrated around the longitudinal plasmon resonance of nanorods at longer wavelengths. This is the closest situation to the behavior of a fluorophore, in which the Stokes-shifted emission can be easily detected by introducing a long-pass filter. The drawback, however, is that the cross section of particles is much smaller at this wavelength and can only be compensated by increasing the excitation power.

Figure 4.1 shows typical spectra of a gold nanorod under different excitation wavelengths. The green curve is the one-photon-excited luminescence spectrum around the longitudinal plasmon resonance, observed while irradiating with 532 nm laser; the full spectrum of the longitudinal plasmon is clearly observable with its resonance at 620 nm. The particle can also be excited at or close to its resonance, where its absorption cross

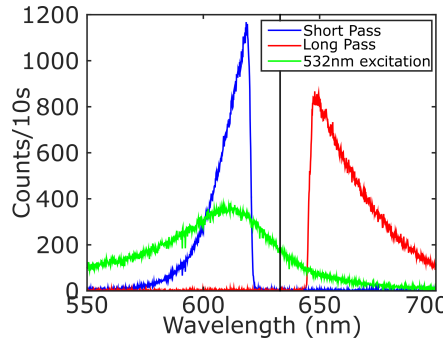


Figure 3.1: Luminescence spectra of a single gold nanorod. Green curve: emission upon excitation with a 532nm laser. Red curve: Stokes emission upon excitation with a resonant 633nm HeNe laser. Blue curve: anti-Stokes emission under the same 633nm excitation.

section is maximum.

Figure 4.1 shows the emission spectra upon excitation at 633nm, depicted as the vertical black line. The red curve is the Stokes-shifted emission; the spectral shape of this emission overlaps with the one observed exciting at 532nm. Exciting in resonance is more efficient and therefore the emission is much brighter. The blue curve in fig. 4.1 displays the anti-Stokes emission at shorter wavelengths. In this case the spectral shape doesn't resemble that of the plasmon resonance. The exponential-like decay of the anti-Stokes spectrum can be modelled with Boltzmann statistics[24] of the bath (phonons and electrons) energy levels that are present in gold nanoparticles at room temperature. In both cases it is clear from the shape of spectra that the filters block an important part of the emission close to the plasmon maximum.

This work focuses in the exploitation of the anti-Stokes luminescence[25] for imaging of gold nanorods in biologically relevant conditions. This scheme benefits from the enhanced absorption cross section of the particles, their high photo-stability and fairly narrow emission spectra. When exciting in resonance with the plasmon, a short-pass filter can be introduced allowing the observation of only the anti-Stokes emission. This procedure is that it highly reduces the background arising from self-fluorescence and Raman-scattering from cells, most of it being Stokes-shifted. Reducing the background therefore opens the possibility of imaging and tracking smaller particles or using lower excitation powers.

The anti-Stokes emission mechanism[24] is depicted in Figure 3.2 and can be described as follows: an absorbed photon generates a collective oscillation of the conduction electrons. After a fast loss of the coherence[26], the state of the particle can be described as an electron-hole pair. After one or more interactions with the thermal baths, i.e. with phonons of the gold lattice[27] or thermally excited charge carriers[28], the hole and/or the electron can receive energy. This energy can transiently increase the energy difference between electron and hole; if then they recombine radiatively, the emitted photon will have a shorter wavelength (higher energy) than the incoming photon[29]. The same mechanism accounts for the Stokes-shifted emission, the only difference being that the electron-hole pair has lost energy to the baths before recombining radia-

3

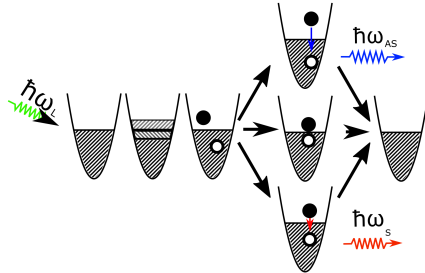


Figure 3.2: Schematic of the anti-Stokes luminescence arising from a single gold nanorod. After excitation with a photon, a collective oscillation of electrons is generated. Once the coherence is lost, the state can be described as an electron-hole pair. Three scenarios are possible: electron and hole may recombine radiatively after one or more interactions with the thermal baths of lattice phonons and charge carrier thermal excitations: i) if the energy difference between electron and hole states is lower than the initial one after excitation we obtain Stokes emission upon a radiative recombination; ii) if electron and hole transiently increase their energy difference at the bath's expense before recombining radiatively, we observe anti-Stokes emission; iii) if electron and hole recombine non radiatively, their energy difference is transferred to the baths and no photon is emitted. The latter process is the most probable one).

tively. Finally, electron and hole can recombine non-radiatively, transferring their whole energy to the lattice.

The probability of a radiative recombination of electrons and holes is low, as can be experimentally determined by the very low emission quantum yield of the photoluminescence[13][20]. Anti-Stokes emission stems from electron-hole recombination events after the electron-hole pair has transiently gained energy from the lattice, i.e., before it thermalizes. Even if the anti-Stokes scenario is unlikely, it is frequent enough as to observe an intensity in the range of 10^3 counts per second on an avalanche photodiode with excitation powers around 16 kW/cm^2 . Such relatively high detection rates require enhancement of the emission probability through the proximity of the plasmon resonance[30].

The main advantage of the approach presented in this work is the simplicity of its implementation. With any confocal or wide-field setup enabling resonant excitation of gold nano-particles, one can exploit the anti-Stokes photoluminescence by inserting a proper short-pass filter in the detection path. As we will see below, single gold nanoparticles can be detected even in higher background conditions such as a stained cell, or a highly self-fluorescent sample.

3.2. EXPERIMENTAL METHOD

Images of gold nanorods were recorded by sample scanning employing a XYZ piezo stage (PI Nano Cube) in a home-built confocal microscope, sketched in Figure B.1a. The objective employed was an oil-immersion Olympus 60X NA 1.4 that allowed a high efficiency in both exciting the particles and collecting their emission. The luminescence arising from the particles was filtered and detected by either an avalanche photodiode or a liquid-nitrogen-cooled CCD-spectrometer (Acton 500i). An example of an image can be seen in Figure B.1b. To detect the anti-Stokes luminescence, a 633 nm short-pass filter (Semrock) was added to the detection path together with a 633 nm notch filter. Both

filters were needed simultaneously since neither of them was able to entirely block the excitation light from the detectors. The Stokes luminescence was collected replacing the short-pass filter with a 633 nm long-pass (Semrock).

Gold nanorods were synthesized by following the standard seeded-growth method[22]. The average size of the nanorods was $50\text{ nm} \times 23\text{ nm}$ and their SPR was located at around 630 nm in water. Figure B.2 shows the extinction spectrum of a suspension of the nanoparticles after synthesis and Fig. B.4 shows a TEM image of the rods.

Two different laser wavelengths were employed. A 532 nm laser (CNI) was used to excite the transverse plasmon and the full longitudinal plasmon spectrum was collected. Single nanorods exhibit a narrow Lorentzian-shaped luminescence spectrum as displayed in Figure B.1c. A second laser (Thorlabs HeNe) with a wavelength of 633 nm allowed us to excite the particles in resonance and collect either the Stokes or the anti-Stokes emission depending on the analysis filters.

3

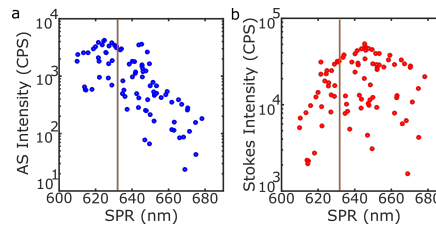


Figure 3.3: Emission intensity of different gold nanorods as a function of their plasmon peak position. The data are plotted for the anti-Stokes (a) and Stokes (b) sides of the emission; the orange vertical line at 633 nm is the wavelength of the laser. The spread in intensities for similar peak positions can be attributed to variations in sizes and, possibly, to different quantum yields of the different individual particles. The maximum emission for the anti-Stokes is obtained when the plasmon is slightly blue shifted from the excitation laser and viceversa for the Stokes emission.

Figure 3.3 shows a scatter plot of the Stokes and anti-Stokes emission intensities of 75 gold nanorods against their plasmon peak position. The large dispersion of the points observed can be attributed to the distribution of sizes of the rods inherent to the synthesis method[31] (bigger particles will have a bigger cross section) and probably to different photoluminescence quantum yields for different individual particles. Because the particles were first deposited on glass directly and because they were excited with circularly polarized light, their orientation shouldn't influence their photoluminescence intensity. It is possible to observe that the maximum emission intensity for the anti-Stokes appears for those particles with their plasmon slightly blue-shifted from the laser wavelength, while the opposite is observed for the Stokes emission. This means that there is a trade-off between the excitation efficiency and the collection efficiency: exciting in perfect resonance is more efficient, but the filters will eliminate most of the luminescence. Therefore exciting slightly to the blue (red) of the resonance will be beneficial for the (anti-)Stokes imaging.

To prove that the technique is well suited for imaging particles in biological systems, we deposited HeLa cells on top of the nanorod sample. Firstly, nanoparticles were deposited on clean glass coverslips by spin casting a suspension of gold nanorods as described elsewhere[31]. This procedure ensures that the analysis is performed on single

nанородов и поэтому что светящиеся сигналы не возникают из кластеров нанородов. Это также позволило нам характеризовать излучение нанородов как путем получения спектров, так и путем изучения зависимости с экспозиционной мощностью, избегая диффузии вдали от фокуса.

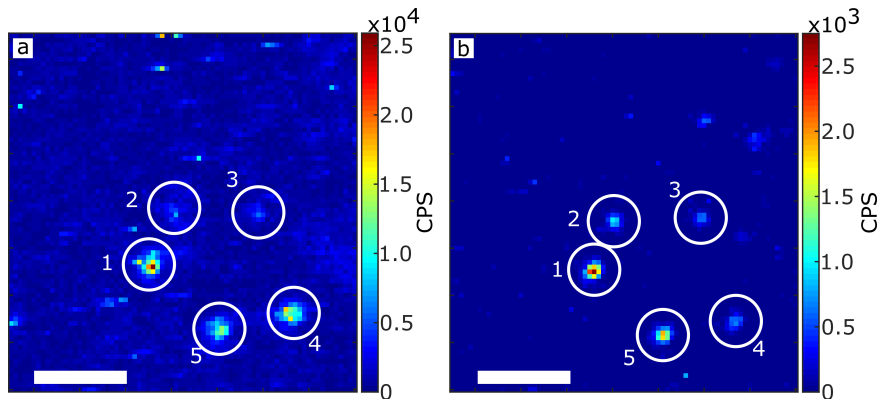
Второй этап: HeLa клетки были высажены на эти образцы и выращены на ночь до высокой конденсации. Хотя полученные изображения не эквивалентны изображениям золотых нанородов, находящихся в цитоплазме или ядре клеток, они будут похожи на изображения рогов в мембранах клеток. Этот упрощенный протокол служит для настоящей цели оптической сигнально-фоновой характеристики, и избавляет нас от трудоемкой био-совместимой функционализации частиц, которая потребовалась бы для более применимых биологических исследований. На рисунке B.5 показано типичное изображение белого света передачи изображения образцов. Высокая конденсация гарантирует, что клетки равномерно покрывают весь наблюдаемый участок, так что изучаемые нанороды всегда локализованы под клеткой. Мы также получили изображения наночастиц под клетками, содержащими флуоресцентный краситель ATTO 647N. Для этого назначения клетки, уже прикрепленные к предметным стеклам, были инкубированы с 45 пМ ATTO 647N в течение приблизительно двадцати минут. Этот набор экспериментов позволил нам сравнить Stokes и anti-Stokes излучения при высоком фоне.

3.3. RESULTS AND DISCUSSION

Наночастица, показанная на рисунке 4.1, демонстрирует сопоставимые коэффициенты счета для обоих Stokes и anti-Stokes излучений. Как было объяснено ранее и показано на рисунке 3.3, это потому, что возбуждающий лазер слегка красно-смещенный от пласмонного резонанса, самой выгодной позиции для усиления anti-Stokes части спектра. Оба типа излучения также сопоставимы с интенсивностью светящегося излучения, полученного при возбуждении на 532 нм. Основное различие в интенсивности лазера; плотность мощности для возбуждения трансверсального пласмона с 532 нм лазером установлена на 80 кВт/см², в то время как для обоих anti-Stokes и Stokes, 633 нм лазер был установлен на 15 кВт/см², в 5 раз менее интенсивен. Это предполагает, что усиление поглощения крестового сечения на резонансе компенсирует потерю значительной части светящегося излучения в лазерном отсеивателе, позволяя использовать меньшие мощности.

Три кривые на рисунке 4.1 также показывают very distinctive spectral distribution. The luminescence that arises from the 532 nm excitation spans almost 150 nm, from the laser wavelength up to more than 650 nm. The Lorentzian shape confirms that the emission arises from a single nanorod. The long-pass emission (red curve) spans a range of almost 100 nm, from the excitation at 633 nm to above 700 nm. Finally, the anti-Stokes emission, which requires energy extraction from the thermal bath cannot extend much beyond a few k_BT from the excitation energy. This is the narrowest band, extending from the excitation to about 580 nm. The position of the plasmon resonance to the blue of the excitation laser explains the higher peak intensity of the anti-Stokes spectrum compared to the Stokes spectrum, whereas the total integrated Stokes emission is higher than the anti-Stokes's.

На рисунке 3.4 показаны два скана растра того же 7.5 × 7.5 μm² участка образца с HeLa клетками на золотых нанородах. Левое изображение показывает Stokes излучение, где 633 nm notch и 633 nm long pass filter были применены. Правое изображение соответствует anti-Stokes излучению, где same notch и 633 nm short pass filter были применены.



3

Figure 3.4: Raster scan of a nanorod sample under HeLa cells using (a) a long pass filter and (b) a short pass filter for photoluminescence detection. Some rods can be observed in both images, some others only in the Stokes or anti-Stokes images. Intensities in the Stokes and anti-Stokes emission thus do not necessarily correlate. The scale bar in both figures is $2\text{ }\mu\text{m}$ in length.

employed. In both cases the irradiation intensity was kept at 30kW/cm^2 at the back aperture of the objective. Most particles are observed in both Stokes and anti-Stokes images but with different intensities. The main difference between the two images is the background count rate. The Stokes image has an average count rate around 5kCPS , while the anti-Stokes is below 100 CPS , close to the dark counts of the detector. Moreover in the Stokes image a structured background can be observed; we attribute this emission to self-fluorescence of the cells. On the other hand, the anti-Stokes image shows a much flatter background and highly distinguishable single particles. Both images display the count rate obtained after dark count subtraction.

The circled particles in fig. 3.4 show the different possible situations: Particle 1 is the brightest both in Stokes and anti-Stokes and can be explained if this is a bigger particle. Particles 2 and 3 are barely distinguishable in the Stokes image, while they are clearly visible in the anti-Stokes. This can be attributed to a higher background level in the Stokes case and by a plasmon resonance of particles 2 and 3 to the blue of the laser, favoring the anti-Stokes emission process. Particles 4 and 5 are visible in both, but particle 4 is brighter than 5 in the Stokes image, while the opposite happens in the anti-Stokes. This is due to a plasmon position that favors more one or the other type of emission, as also shown in fig. 3.3. Figure B.6 shows a larger area of the scan, where it is possible to observe more particles both in the Stokes and anti-Stokes configuration.

The use of the anti-Stokes emission is highly especially valuable when imaging nanoparticles in high background conditions. To this end we incubated the cells with a solution of ATTO 647N. The fluorescent labelling of the cell, even if not specific, resulted in a similar situation to what would be obtained in the case of labelling organelles or the entire cell membrane. This dye was chosen because its absorption maximum is close to 633 nm , the excitation wavelength we employed in these experiments, but also because of its photostability and high quantum yield.

Figure 3.5 shows two raster scans of the samples described above. The right panel

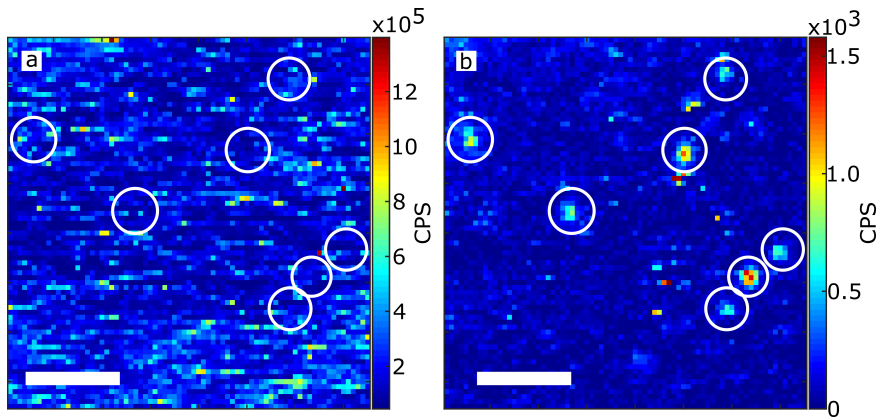


Figure 3.5: Raster scan of a nanorod sample covered by HeLa cells containing the fluorescent dye ATTO 647N, again using (a) a long pass filter and (b) a short pass filter for photoluminescence detection. No clear nanorod signals can be seen in the Stokes images, whereas they are clearly distinguishable in the anti-Stokes image, proving the advantage of the latter for fluorescence background rejection. The scale bar in both figures is $2\mu\text{m}$ in length.

shows the anti-Stokes image, in which single particles are clearly distinguishable and marked with a circle. We made sure that the observed spots were nanorods by monitoring their intensity under high illumination conditions and checking that they did not bleach. The left panel shows the Stokes emission, in which no particles can be distinguished from the background. The average emission in the anti-Stokes image is below 500CPS, but higher than the dark counts of the detector. The Stokes emission, on the other hand shows an average intensity around 200kCPS, one order of magnitude higher than that observed without the dye.

These results indicate that the Stokes image deteriorates much faster than the anti-Stokes in the presence of emitting molecules both from the cell itself or from added dyes. The images show regions with higher emission intensities in both configurations, most probably due to a higher concentration of dye in specific regions of the cell. Figure B.7 shows a larger scan, and the difference in background intensities is more evident. At much higher concentrations than the ones shown in this work, the anti-Stokes emission from the dye becomes significant and can overcome the emission rate from individual particles.

Figure 3.6a shows the dependence of the acquired luminescence and the background as functions of excitation power for both the Stokes and anti-Stokes emissions of a particle below a cell without dye. Care was taken in choosing a particle with a resonance close to the excitation laser, to compare Stokes and anti-Stokes luminescence with similar resonant enhancements. The Stokes emission (red curves) shows a linear increase in signal together with a linear increase in background. In this case the signal-to-background ratio reaches a value of 6. The anti-Stokes emission (blue curves) however shows a much steeper increase of the signal than the background, reaching a signal-to-background ratio of 12. Of course, particles with a plasmon resonance to the blue of the laser wavelength show an even larger ratio of anti-Stokes to Stokes emission.

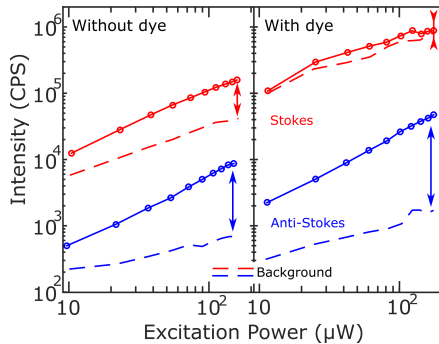


Figure 3.6: Emission intensity (solid lines) and background (broken lines) as functions of excitation intensity for the Stokes (red) and the anti-Stokes (blue) emissions. These data were obtained on two different particles for the right (unstained cells) and left (stained cells) panels. For the unstained cells, the plasmon was chosen close to the laser line, so as to avoid favouring one or the other emission by the resonance effect. Arrows indicate the maximal signal-to-background ratio of each emission in the figure conditions.

Figure 3.6b shows the same type of curves as 3.6a, for a different particle under cells that contained ATTO647N. In this case the background prevented the acquisition of luminescence spectra; the particle chosen to draw the figure is representative of the average behavior. We see that in the Stokes case the particle's signal is barely larger than the fluorescence background from the dye. On the other hand, the anti-Stokes luminescence shows an enhanced contrast, reaching a signal-to-background ratio of more than 20 for this particular nanorod. The background level observed in the Stokes image increases much faster with dye content than the anti-Stokes background.

When the cells containing ATTO647N were used, we observed an increase in the background levels for both Stokes and anti-Stokes emission and these levels also depend on excitation power. This means that the dye shows both components, as is well known from fluorescence hot bands and anti-Stokes Raman scattering. The main difference between nanoparticles and dyes, however, is their quantum yield. While the particles appear to be relatively bright anti-Stokes emitters, in part due to their large absorption cross section, in part due to their plasmon resonance, dyes such as the one employed in this work, are much better Stokes emitters than anti-Stokes. This is the main reason why rods are drowned by the fluorescence background in the Stokes image.

The signal-to-background ratio of the anti-Stokes emission increases with increasing laser excitation powers, going from values close to 2 for $3\text{ kW}/\text{cm}^2$ excitation up to values of 20 for $53\text{ kW}/\text{cm}^2$ as shown in fig 3.6b. However this can't be extrapolated further than the results presented here. It is known that gold nanorods reshape under high irradiation intensities[32]. For high-NA objectives like the one employed in this work, a rule of thumb to prevent reshaping in scanning confocal images is to keep the excitation intensity lower than $150\text{ }\mu\text{W}$ at the back aperture of the objective lens (or equivalently a power density of $53\text{ kW}/\text{cm}^2$ at the object plane.)

In the presence of a fluorescent dye, the signal-to-background obtained is higher than in the case without dye. This may be a consequence of the selection of particles with a plasmon more favorable to the anti-Stokes than to the Stokes emission, and

couldn't be avoided by acquiring luminescence spectra since the background was too high. Although we checked the correct focusing on the sample plane both by optimizing the reflection on the glass/water interface and by employing the anti-Stokes signal, it was never possible to observe single particles under high background conditions in the Stokes configuration.

3.4. CONCLUSIONS

In this work we have demonstrated that anti-Stokes photoluminescence arising from the excitation in (or close to) the plasmon resonance of a gold nanorod can be exploited to image them in biologically relevant conditions[25]. The comparison between the Stokes and anti-Stokes emissions was possible by using particles immobilized on the substrate, but this work shows that the technique can be easily extended to imaging in fixed cells, *in vivo* or even for tracking particles in real time[6].

Extending this technique to wide-field should be possible considering the laser powers employed in this work. EMCCDs provide enough gain[33] to easily detect single nanoparticles, while at the same time the background is sufficiently low to give a high contrast. This extension of the technique would open the possibility to track at higher frame rates than achievable by confocal imaging.

The lower count rate of the anti-Stokes compared to the Stokes emission can be a drawback in such applications as localization[34]. This technique's accuracy depends on the number of photons detected, and is given by $\approx 1/\sqrt{N}$, where N is the number of photons collected. The count rates obtained in this work are close to 1.5kCPS, enough in many applications.

We have shown that the signal-to-background ratio of the anti-Stokes emission is higher than that of the Stokes emission. In the case of HeLa cells not containing a fluorescent dye, typical values can be around 10 and 5 respectively for a particle with a resonance at the laser wavelength. For HeLa cells containing ATTO647N the difference is much more pronounced, since most of the particles will have a Stokes emission comparable or lower than the background, while in the anti-Stokes the signal-to-background ratio can still be higher than 10.

The main advantage of the technique presented in this work is that it can be easily implemented in any commercial or home-built microscope. It does not require a high investment in equipment or time, since filters are normally available for common laser wavelengths and there is no further need of modifying any experimental configuration already existent. Moreover all the data analysis techniques employed in confocal or wide-field images for localization, tracking, etc. do not have to be modified.

3.5. AUTHOR CONTRIBUTIONS

AC performed the experiments, analyzed data and wrote the article. VIPK prepared the samples and performed the experiments. MJMS designed the study. MO designed the study and wrote the article. All authors analyzed the results and approved the final version of the manuscript.

3.6. ACKNOWLEDGEMENTS

We thank Aimee Boyle for the synthesis and TEM images of the gold nanorods. This work is part of the research programme of the Foundation for Fundamental Research on Matter (FOM), which is part of the Netherlands Organisation for Scientific Research (NWO).

REFERENCES

- [1] W. E. Moerner, *New directions in single-molecule imaging and analysis*, Proc. Natl. Acad. Sci. **104**, 12596 (2007).
- [2] J. W. Lichtman and J.-A. Conchello, *Fluorescence microscopy*. Nat. Methods **2**, 910 (2005).
- [3] N. C. Shaner, P. A. Steinbach, and R. Y. Tsien, *A guide to choosing fluorescent proteins*. Nat. Methods **2**, 905 (2005).
- [4] N. R. Jana, L. Gearheart, and C. J. Murphy, *Wet Chemical Synthesis of High Aspect Ratio Cylindrical Gold Nanorods*, J. Phys. Chem. B **105**, 4065 (2001).
- [5] A. M. Alkilany, L. B. Thompson, S. P. Boulos, P. N. Sisco, and C. J. Murphy, *Gold nanorods: Their potential for photothermal therapeutics and drug delivery, tempered by the complexity of their biological interactions*, Adv. Drug Deliv. Rev. **64**, 190 (2012).
- [6] B. van den Broek, B. Ashcroft, T. H. Oosterkamp, and J. van Noort, *Parallel Nanometric 3D Tracking of Intracellular Gold Nanorods Using Multifocal Two-Photon Microscopy*, Nano Lett. **13**, 980 (2013).
- [7] J. Pérez-Juste, I. Pastoriza-Santos, L. M. Liz-Marzán, and P. Mulvaney, *Gold nanorods: Synthesis, characterization and applications*, Coord. Chem. Rev. **249**, 1870 (2005).
- [8] M. B. Mohamed, V. Volkov, S. Link, and M. A. El-Sayed, *The 'lightning' gold nanorods: fluorescence enhancement of over a million compared to the gold metal*, Chem. Phys. Lett. **317**, 517 (2000).
- [9] S. Yao, H. H. Cai, M. Liu, and P. H. Yang, *Fluorescent labeling of cellular targets and multicolor imaging with gold nanorods*, Dye. Pigment. **101**, 286 (2014).
- [10] K. M. Spillane, J. Ortega-Arroyo, G. de Wit, C. Eggeling, H. Ewers, M. I. Wallace, and P. Kukura, *High-speed single-particle tracking of GM1 in model membranes reveals anomalous diffusion due to interleaflet coupling and molecular pinning*. Nano Lett. **14**, 5390 (2014).
- [11] A. S. Urban, T. Pfeiffer, M. Fedoruk, A. a. Lutich, and J. Feldmann, *Single-step injection of gold nanoparticles through phospholipid membranes*. ACS Nano **5**, 3585 (2011).

- [12] N. Lewinski, V. Colvin, and R. Drezek, *Cytotoxicity of nanoparticles*, Small **4**, 26 (2008).
- [13] M. Yorulmaz, S. Khatua, P. Zijlstra, A. Gaiduk, and M. Orrit, *Luminescence quantum yield of single gold nanorods*. Nano Lett. **12**, 4385 (2012).
- [14] S. Link, M. B. Mohamed, and M. a. El-Sayed, *Simulation of the optical absorption spectra of gold nanorods as a function of their aspect ratio and the effect of the medium dielectric constant*, J. Phys. Chem. B **103**, 3073 (1999).
- [15] S. Berciaud, D. Lasne, G. Blab, L. Cognet, and B. Lounis, *Photothermal heterodyne imaging of individual metallic nanoparticles: Theory versus experiment*, Phys. Rev. B **73**, 045424 (2006).
- [16] F. Ignatovich and L. Novotny, *Real-Time and Background-Free Detection of Nanoscale Particles*, Phys. Rev. Lett. **96**, 013901 (2006).
- [17] A. Bouhelier, R. Bachelot, G. Lerondel, S. Kostcheev, P. Royer, and G. P. Wiederrecht, *Surface Plasmon Characteristics of Tunable Photoluminescence in Single Gold Nanorods*, Phys. Rev. Lett. **95**, 267405 (2005).
- [18] E. Dulkeith, T. Niedereichholz, T. a. Klar, J. Feldmann, G. Von Plessen, D. I. Gittins, K. S. Mayya, and F. Caruso, *Plasmon emission in photoexcited gold nanoparticles*, Phys. Rev. B - Condens. Matter Mater. Phys. **70**, 1 (2004).
- [19] S. Link and M. a. El-Sayed, *Int. Rev. Phys. Chem.*, Vol. 19 (2000) pp. 409–453.
- [20] W. Rao, Q. Li, Y. Wang, T. Li, and L. Wu, *Comparison of Photoluminescence Quantum Yield of Single Gold Nanobipyramids and Gold Nanorods*, ACS Nano **9**, 2783 (2015).
- [21] L. L. T. Ngoc, J. Wiedemair, A. van den Berg, and E. T. Carlen, *Plasmon-modulated photoluminescence from gold nanostructures and its dependence on plasmon resonance, excitation energy, and band structure*, Opt. Express **23**, 5547 (2015).
- [22] B. Nikoobakht and M. A. El-Sayed, *Preparation and Growth Mechanism of Gold Nanorods (NRs) Using Seed-Mediated Growth Method*, Chem. Mater. **15**, 1957 (2003).
- [23] W. Ni, X. Kou, Z. Yang, and J. Wang, *Tailoring longitudinal surface plasmon wavelengths, scattering and absorption cross sections of gold nanorods*, ACS Nano **2**, 677 (2008).
- [24] Y. He, K. Xia, G. Lu, H. Shen, Y. Cheng, Y.-c. Liu, K. Shi, Y.-F. Xiao, and Q. Gong, *Surface enhanced anti-Stokes one-photon luminescence from single gold nanorods*, Nanoscale **7**, 577 (2015).
- [25] L. Jiang, I. W. Schie, J. Qian, S. He, and T. Huser, *Coherent anti-Stokes emission from gold nanorods and its potential for imaging applications*. Chemphyschem **14**, 1951 (2013).

- [26] C. Sönnichsen, T. Franzl, T. Wilk, G. von Plessen, J. Feldmann, O. Wilson, and P. Mulvaney, *Drastic reduction of plasmon damping in gold nanorods*. Phys. Rev. Lett. **88**, 077402 (2002).
- [27] Z. Lin, L. V. Zhigilei, and V. Celli, *Electron-phonon coupling and electron heat capacity of metals under conditions of strong electron-phonon nonequilibrium*, Phys. Rev. B - Condens. Matter Mater. Phys. **77**, 1 (2008).
- [28] C. K. Sun, F. Vallée, L. H. Acioli, E. P. Ippen, and J. G. Fujimoto, *Femtosecond-tunable measurement of electron thermalization in gold*, Phys. Rev. B **50**, 15337 (1994).
- [29] J. Huang, W. Wang, C. J. Murphy, and D. G. Cahill, *Resonant secondary light emission from plasmonic Au nanostructures at high electron temperatures created by pulsed-laser excitation*. Proc. Natl. Acad. Sci. U. S. A. **111**, 906 (2014).
- [30] B. Neupane, L. Zhao, and G. Wang, *Up-Conversion Luminescence of Gold Nanospheres When Excited at Nonsurface Plasmon Resonance Wavelength by a Continuous Wave Laser*. Nano Lett. (2013), 10.1021/nl401505p.
- [31] P. Zijlstra and M. Orrit, *Single metal nanoparticles: optical detection, spectroscopy and applications*, Reports Prog. Phys. **74**, 106401 (2011).
- [32] Y. Liu, E. N. Mills, and R. J. Composto, *Tuning optical properties of gold nanorods in polymer films through thermal reshaping*, J. Mater. Chem. **19**, 2704 (2009).
- [33] D. Dussault and P. Hoess, *Noise performance comparison of ICCD with CCD and EMCCD cameras*, Opt. Sci. Technol. SPIE 49th Annu. Meet., , 195 (2004).
- [34] S. J. Sahl and W. E. Moerner, *Super-resolution fluorescence imaging with single molecules*. Curr. Opin. Struct. Biol. **23**, 778 (2013).



4

GOLD NANOPARTICLES AS NANO-THERMOMETERS

This is the abstract

4.1. INTRODUCTION

Many physical, chemical, biological processes depend on temperature. Together with the miniaturization of devices and the advent of nanotechnology the need for measuring temperature with high spacial accuracy started to emerge. Notably in biology[1, 2] and medicine[3] measuring and controlling temperature at a single cell level will provide not only insight into intracellular processes but it will also contribute to a better understanding of the mechanisms involved in the proposed new therapies such as photothermal tumor ablation[4] or controlled drug delivery[5][6].

Probes with distinctive spectral features are ideal candidates for temperature measurements since they provide high spatial accuracy while far field optics allow a non contact readout. Some of the proposed strategies include structures that undergo a conformational change at different temperatures[7], thus inducing a change in fluorescence intensity of a dye molecule embedded into them. Also cleverly designed fluorescent probes[8] in which the ratio of particular emission peaks depend on temperature allow a high accuracy and can be used for intracellular thermometry.

The use of anti-Stokes fluorescence emission from molecules yields a high temperature accuracy[9]. However organic dyes show a very low amount of emitted photons with a higher energy than the excitation energy, rendering very challenging their use in biological conditions. Recently Surface Enhanced Raman Spectroscopy (SERS) allowed to address the changes induced by temperature down to single-molecules[10], but a careful calibration of the measurements is crucial.

At a cellular level there is an open debate regarding the measured temperatures in cells since they are in the order of 10^5 times higher than the expected values drawn from theoretical models[1, 11]. Moreover new applications in photothermal therapy re-

quire locally increasing the temperature in order to induce the death of specific cells in a tissue[12][5]. Many of this methods employ metallic nanoparticles as heat sources[4][13] but rely on models[14] or in ad-hoc calibrations to estimate the reached temperatures[15]. Therefore a method that allows both to increase the local temperature and to monitor it will be of great interest in a broad range of fields.

Gold nanoparticles continue to receive a great amount of attention because of their optical properties[16]. A large absorption and scattering cross section spanning through almost the entire visible spectrum makes them easy to detect via exciting their luminescence and collecting either the Stokes or the anti-Stokes emission[17]; in a dark field scattering[18] configuration or via photothermal imaging[19]. Moreover their signal is stable over time; gold nanoparticles do not blink nor bleach, making them ideal candidates for biological labeling.

4

Different metallic nano-objects are being introduced as agents for photothermal therapy or drug delivery[20]. One of the advantages of gold nanoparticles is the possibility of tuning their resonance to the near infra-red range, where the penetration of light into tissues can be of several centimeters[3–5, 12, 13, 21]. Moreover the particles can be used not only for treatment, but also for imaging. In this work we propose that the anti-Stokes luminescence of gold nanorods and nanospheres can be used to measure their temperature with a relatively high accuracy.

Luminescence of metallic nanoparticles has been object of extensive study in recent years. Since the first observation of luminescence from bulk gold[22], different groups have tried to quantitatively describe the observed properties[23, 24], as the quantum yield[25–28] and the emission spectrum[29]. Several computer packages[30] allow to compute the cross sections of different geometries and there are already several successful applications of nanoparticles into different fields. The anti-Stokes emission from these particles has however been largely overlooked.

The mechanism we propose to explain the luminescence from gold nanoparticles is based in the radiative recombination of electron and holes that are created upon the absorption of an incident photon[22, 31]. The emission will be enhanced by the presence of the surface plasmon acting as an antenna[23]. At the same time, the probability of the interaction of the electron or hole with a phonon before recombining can give rise to an emission photon with a higher energy than the excitation[32–34].

A monochromatic photon incident to the particle will give rise to a collective oscillation of the gas of conduction electrons. The coherence of the oscillation is broken due to collisions with the particle's surface and to the interaction with baths[35, 36]. These can be mainly the electron-electron interactions, electron-phonon coupling and the bath of photons coupled via spontaneous emission. The decoherence time can be measured in pulsed experiments or deduced from the inverse linewidth of the plasmon resonance and is in the order of 6fs or shorter[37]. After this the state of the system can be described as a superposition of hot electron and hole states.

The hot electron and hole cool down by exchanging energy with the lattice on a timescale of $\tau \approx 1\text{ ps}$ [38]. Before this happens, electron and hole have a small probability of recombining radiatively, re-emitting their high electronic energy as a photoluminescence photon. If they have interacted only with static surfaces, their energy would be the same and therefore the emitted photon would have the same energy than the incoming

photon, and will not contribute to the measured photoluminescence (will be blocked by the notch filter.) If on the other hand they have interacted with a phonon they have lost or acquired a phonon energy and momentum quantum before recombining.

Electron and hole can also interact with phonons upon recombination, either by creation or annihilation of a phonon. In both cases the energy available upon recombination cannot exceed $\hbar\omega_L + k_B T$. It has to be noted that in the hypothesis of a single-photon absorption, i.e. at low excitation power, the temperature T is that of the bath before absorption, the temperature of the surrounding medium of the particle. This is different from pulsed experiments, in which the electron gas temperature can be orders of magnitude higher than room temperature[39].

Radiative recombination gives rise to weakly emitting sources spatially and spectrally distributed throughout the particle over a broad frequency band with an exponential cutoff at $\hbar\omega_L + k_B T$. The weak recombination emission can be greatly enhanced by the surface plasmon resonance, acting as an antenna. With this model the following prediction can be made. Firstly the emission spectrum must follow the plasmon spectrum if the excitation laser is well above the plasmon resonance as shown in Figure 4.1 in the results. If the excitation falls within the plasmon resonance, the spectrum is expected to follow the plasmon spectrum multiplied by Bose-Einstein statistics factor arising from phonon population. This factor should be proportional to \bar{n} for anti-Stokes and $\bar{n} + 1$ for Stokes processes, where

$$\bar{n} = \left(\exp \frac{\hbar\Omega}{k_B T} - 1 \right)^{-1}. \quad (4.1)$$

With this model, it can also be predicted that the emission should be polarized as the plasmon; for gold nanorods this polarization coincides with the longitudinal axis of the particle[40]. Moreover, the lifetime should be determined by the lifetime of hot electrons and holes and should be significantly shorter than the thermalization time of the carriers. If this was not the case, few interactions with phonons are enough to reduce the carriers' energy and therefore the electron and hole wouldn't have enough energy to produce an optical photon. Finally in the model only the presence of hot carriers is required. As the wavevectors are randomly distributed at all times, the recombination probability remains constant at all stages of relaxation. Therefore excitation well above the plasmon resonance should excite the photoluminescence with nearly the same efficiency as just above the plasmon resonance.

In this work we propose to use the anti-Stokes luminescence emission from gold nanoparticles to determine their temperature. According to the model just described, the anti-Stokes emission follows the following form,

$$I(\nu) = SPR(\nu) \cdot \left(\exp \frac{h(\nu - \nu_L)}{k_B T} - 1 \right)^{-1} \quad (4.2)$$

where I is the intensity, ν is the frequency of the photons, SPR is the surface plasmon resonance, ν_L is the frequency of the laser, h is Planck's constant, k_B the Boltzmann constant and the only remaining free parameter is the Temperature T (plus a normalization constant not included in eqn. 4.2.) This means that carefully fitting the emission spectra

allows to extract the absolute temperature of the particles without any previous calibration.

4.2. EXPERIMENTAL METHOD

All the measurements in this work were performed in a home-built confocal microscope equipped with an APD and a spectrometer (Acton 500i). Samples were mounted in a flowcell that allowed to increase the temperature of the medium up to 60 °C and to monitor it through a Pt100 resistance thermometer placed 1 mm away from the observation area.

Samples were prepared by spin casting a suspension of nanoparticles onto clean coverslips. Different particles were employed in this work. Nanorods with average dimensions of 21 nm × 50 nm and a plasmon resonance around 650 nm were synthesized following the seeded-growth method; spheres with radii between 30 nm and 60 nm were purchased from BBI International. We employed a 532 nm (CNI) laser for characterizing the nanorods' plasmon and for exciting spheres close to resonance. A 633 nm HeNe (Thorlabs) was employed to excite the nanorods in resonance.

Room temperature measurements were performed using a 60X, NA 1.4 oil immersion objective (Olympus). This allowed a high excitation and collection efficiency. At higher temperatures a dry objective, 60X, NA 0.9 (Olympus) was employed to avoid the presence of a heat-sink directly in contact to the observed area. The lower NA of this objective made both the excitation and collection efficiencies significantly lower. The first can be compensated increasing the excitation power, the latter however is inherent to the method and can be compensated by increasing the exposure time.

To compensate for the drift of the setup while increasing the temperature, a computer program was developed to continuously track a reference particle. The same program was responsible for recording the temperature and triggering the spectrometer. In this way complete data sets were acquired at different temperatures, including spectra while exciting at 532 nm, at 633 nm with different laser intensities and the temperature measured by the Pt100. A spectrum with the 532 nm laser was taken after every cycle to ensure that the particle was not reshaping due to higher excitation powers.

The intensity of the lasers was controlled via the voltage applied to an AOM in each optical path. Several accumulations of the spectra at the same laser intensity were recorded. On one hand this allowed to lower the noise of the measurements. On the other also allowed to remove bright pixels generated by cosmic rays and to monitor changes in the intensity of the spectra during the acquisition. These changes can be due to a drift of the setup while measuring or to a reshape of the particle, that can be confirmed by comparing the spectra acquired with the 532 nm laser. In case of a recorded intensity change larger than acceptable, the particular spectra was disregarded.

To calculate the heating of the particles the absorption cross section has to be computed. For the case of nanorods, the ADDA package was employed. Spheres' cross section can be calculated from Mie theory. Once the dissipated power is known, the parameters can be either used in a Comsol model or the heat equation can be analytically solved, approximating the rods by spheres of the same volume.

4.3. RESULTS

4

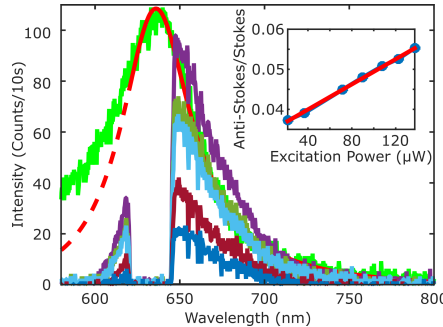


Figure 4.1: Luminescence spectra of a single gold nanorod. The green curve is the emission under 532 nm excitation. In red is the fitting by a lorentzian; the dashed part is the region that was not considered for the fitting. The other curves are the emission of the same particle under 633 nm irradiation at five different powers. The inset shows the anti-Stokes-to-Stokes ratio as a function of the excitation power, overlapped with a linear fit in red.

The proposed model for the anti-Stokes emission requires to know the plasmon spectrum (*SPR* function in equation 4.2) of the particle in order to fit the emission at shorter wavelengths and extract its temperature. It has been shown that both scattering and luminescence spectra overlap over a broad range of wavelengths[27]. Therefore exciting gold nanorods with 532 nm allows to record the longitudinal plasmon spectra, as shown in the green solid curve of Figure 4.1. The peak was fitted by a single lorentzian, shown in red in the Figure; the dashed part of the curve depicts the spectral region that was not considered for the fitting. It has to be reminded that the luminescence spectra is not a perfect lorentzian since there is a broadband contribution to the lumienescence arising between the excitation wavelength and the plasmon peak[41]. This appears as an asymmetry in the emission spectrum, particularly visible for wavelengths smaller than 625 nm. The results of this fitting will be employed for the SPR function defined in equation 4.2. A lengthier discussion on the effects of this procedure will be given later.

The other curves in Fig. 4.1 show the luminescence emission of the same nanorod while irradiating with a 633 nm laser at different powers, ranging from $25 \mu\text{W}$ to $125 \mu\text{W}$ at the back aperture of the objective. The vertical black line shows the wavelength of the laser. The Stokes part of the spectrum at longer wavelengths than the excitation, show the same shape than the plasmon emission observed under 532 nm excitation, besides for a normalization factor. From the figure it can readily be seen that the shape of the anti-Stokes emission, at shorter wavelengths than excitation, is exponential-like and doesn't follow the lorentzian shape of the Stokes emission. The dip between Stokes and anti-Stokes is caused by the notch filter that prevents direct excitation light from reaching the detectors.

The inset of Fig. 4.1 shows the anti-Stokes-to-Stokes ratio of the integrated luminescence for different laser excitation intensities. It is possible to see that even with a linear behavior, the anti-Stokes intensity increases more rapidly with laser excitation power than the Stokes emission. This phenomenon was already exploited to image gold

nanorods in high-background conditions. Moreover it shows that the anti-Stokes emission depends on laser excitation power differently than its Stokes counterpart.

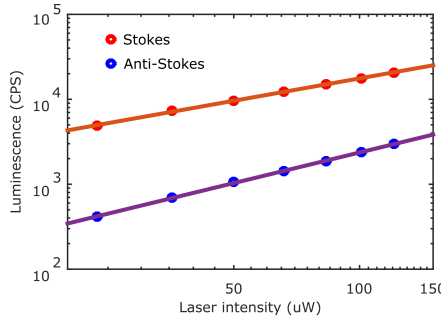


Figure 4.2: Stokes and anti-Stokes emission as a function of excitation power. The linear fit in logarithmic scale has a slope of 0.9 and 1.2 respectively, ensuring the 1-photon nature of both kinds of emission.

Figure 4.2 shows the intensity of the Stokes (red) and anti-Stokes (blue) emission for several excitation powers. In both cases the linear fit in logarithmic scale has a slope close to 1, being 0.9 for the Stokes and 1.2 for the anti-Stokes, ensuring that both types of emission are single-photon processes. The behavior is independent of the plasmon resonance position. It is important to note that the excitation intensity cannot be increased much beyond what is shown because nanorods would start reshaping into spheres given enough laser power.

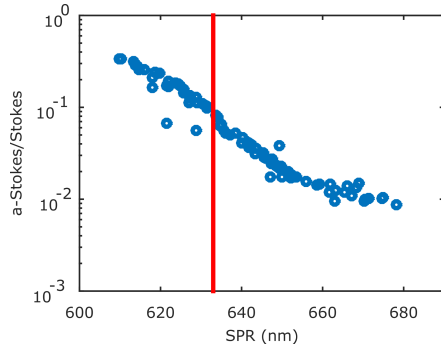


Figure 4.3: Ratio of the anti-Stokes to Stokes emission as a function of the resonance position for 90 different particles under 633 nm irradiation at 100 μW . The red line shows the position of the laser.

Figure 4.3 shows the ratio of the anti-Stokes emission to the Stokes emission for 90 nanorods with different plasmon resonance and under the same 633 nm excitation. The vertical red line depicts the laser wavelength. It can be seen that the maximum ratio happens when the laser is red-detuned from the resonance. This is the case where the plasmon is enhancing preferably the anti-Stokes emission. It has to be kept in mind that off-resonance the cross section is lower and therefore the excitation is not as efficient. Particles with a resonance at the laser wavelength in which nor the anti-Stokes nor the Stokes is preferred, show a ratio close to 10%.

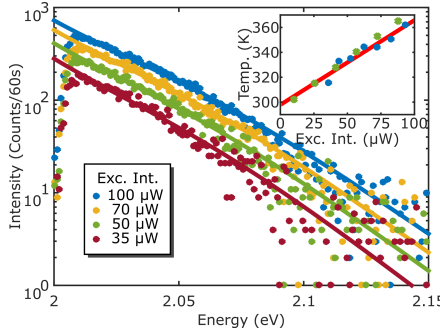


Figure 4.4: Anti-Stokes emission at different irradiation powers with the corresponding fitting by equation 4.2. There is a good overlap between data and model. The inset shows the extracted temperature at each power (blue dots) and a linear extrapolation of the data to $0\mu\text{W}$ excitation power. The value obtained for room temperature was 293 K while the measured value was 296 K. The green stars are the calculated temperatures under the same excitation conditions. There is a good agreement between experimental and numerical values.

4

By fitting the anti-Stokes part of the spectra shown in 4.1 with the equation 4.2 it is possible to extract the temperature of the particle at each excitation power. Figure 4.4 shows the result of this procedure. The spectra shown were recorded at 4 different excitation intensities; the full lines are the fitting results. There is a good agreement between the fitting and the experimental values. The inset in the figure shows the extracted temperatures at different intensities (blue dots). Firstly is possible to observe that the temperature is proportional to the excitation intensity and therefore to the absorbed energy, as expected. From these data is possible to calculate the temperature at $0\mu\text{W}$ excitation power, i.e. room temperature, by extrapolating the results of a linear fit. The obtained value in this case is 293 K, while room temperature was set to 296 K.

To prove that the temperature values obtained with this procedure are reasonable, we performed finite element analysis using Comsol. The cross section was obtained from discrete dipole calculations employing the ADDA package[30]. The values for the dimensions of the particle were deducted from SEM images, and the length was adjusted to obtain a plasmon overlapping to the observed one. The inset in Fig. 4.4 shows the calculated temperatures under the same excitation conditions as the red stars. There is a good agreement between both measurements and simulations. Moreover it can be seen that once calculated the cross section of the particle, the temperature of a rod or of a sphere with the same volume are the same, therefore the temperature can be easily determined from the absorbed power using the heat equation.

As expected from the model, the anti-Stokes emission should depend not only on the particle intrinsic properties but also on the temperature of the surrounding medium[42]. The samples were mounted in a flowcell that allowed to change the temperature and to measure it with a Pt100 resistance thermo detector. It has to be remembered that in this set of experiments we employed a dry objective, and therefore the excitation powers are larger to compensate for the lower excitation efficiency. At each temperature several spectra were acquired at different 633 nm excitation powers and also a spectrum of the plasmon before and after in order to monitor any possible reshaping of the particles during the experiment.

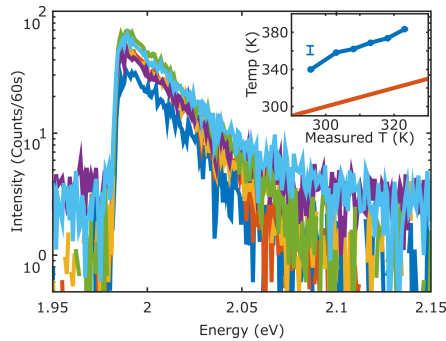


Figure 4.5: Anti-Stokes emission spectra under 633 nm laser excitation at $510 \mu\text{W}$ but at different temperatures. The inset shows the extracted temperature as the temperature of the medium increases.

4

Figure 4.5 shows the anti-Stokes emission spectra at $510 \mu\text{W}$ but at different temperatures. The changes in the slope of the curves encode the different temperatures. The inset in Fig. 4.5 shows the extracted temperature from the fitting with equation 4.2 as a function of the temperature measured by the Pt100 in the vicinity of the nanorod. The red line is showing the water temperature and acts as a guide to the eye.

The inset of Figure 4.5 clearly shows an increase in the extracted temperature while increasing the temperature of the surrounding medium. The range of explored temperatures was from 296K, room temperature, up to 320K. This range is enough to observe a change in the anti-Stokes emission spectrum. At higher temperatures the stability of the setup plays a crucial role in maintaining the particle in focus during the spectra acquisition time. Longer exposure times and therefore lower excitation intensities can be obtained if particles are actively maintained in focus.

Together with the excitation intensity, the plasmon position has a crucial role in the accuracy of the extracted temperature. The luminescence spectrum acquired with the 532nm laser shows an asymmetric shape, due to a broadband contribution from gold added to the plasmonic emission. This makes the initial fitting needed for the SPR function of equation 4.2 non univocally determined. For the particle shown in Fig. 4.1, changing the initial wavelength of the fit from 600nm to 640nm yields a significative difference in the obtained parameters of the lorentzian.

Using the following expression for the SPR function in eV,

$$\text{SPR}(E) = \frac{P_1}{(E - P_2)^2 + P_3}$$

The different fitting ranges give values for P_2 between 1.940 eV and 1.955 eV , while the values of P_3 lie in between $5 \cdot 10^{-3} \text{ eV}^2$ and $8 \cdot 10^{-3} \text{ eV}^2$. Figure 4.6.a shows the extracted temperature difference from the anti-Stokes spectra for all the possible parameter combinations in the range just mentioned. Figure 4.6.b shows the temperature dependence while keeping either P_2 or P_3 constant.

In this example it is possible to note that the extracted temperature is highly dependent on the fitted width of the plasmon spectrum but barely dependent on the extracted peak position. From the initial spectrum of the particle, it is possible to note that the

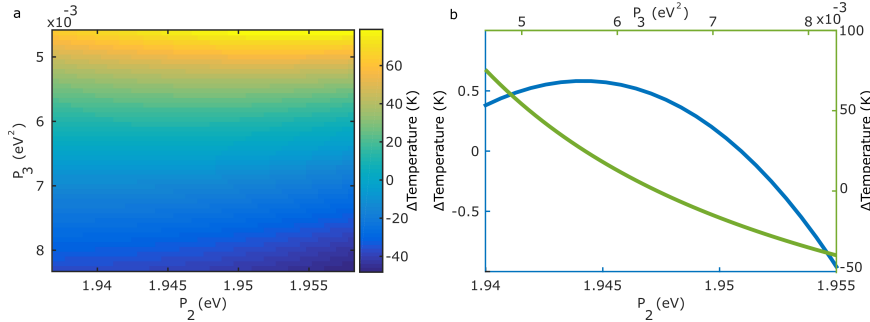


Figure 4.6: Estimation of the error due to different fitting parameters of the plasmon spectrum. a) 2D grid of the difference in temperature obtained while varying both P_2 and P_3 parameters of the fit. b) Temperature dependence while keeping either P_2 or P_3 constant.

4

wing of the plasmon coincides with the range of anti-Stokes emission. Therefore minute changes in the initial shape will yield higher changes in the extracted temperature.

This assertion implies that there should be particles in which the extracted temperature wouldn't be too sensitive to the initial plasmon fit. To explore these possibilities, we calculated the anti-Stokes emission of different particles at 400 K by using equation 4.2 and the results of ADDA calculations for the SPR function. We then extracted a temperature from these spectra while varying the lorentzian parameters as was done for the experimental results. In this way it is possible to study the expected error in temperature generated by the initial uncertainty in the fitting of the plasmon for different particles.

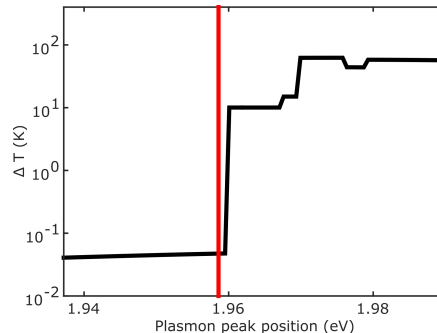


Figure 4.7: Calculated error in the temperature extraction due to the uncertainty in the plasmon parameters as a function of the resonance position of the particle. Clearly, when exciting at the blue wing of the plasmon, the effect of these uncertainties is much lower.

Figure 4.7 shows the uncertainty in the extracted temperature as a function of the plasmon peak position. The uncertainty is defined as the difference of the maximum and the minimum extracted temperatures while varying P_2 by 10% and P_3 by 30%. The vertical red line depicts the position of the laser. It is remarkable the difference for particles with a resonance red-shifted from the excitation laser to particles blue-shifted. Indeed, when the plasmon favors the anti-Stokes emission the correct modelling of the reso-

nance is crucial for the extraction of temperatures. On the other hand, when the plasmon is red-shifted from the excitation, the induced error in the extracted temperature is much lower. The amount of collected light is another factor to keep into account. When the resonance is red-shifted from the laser, the anti-Stokes emission is much weaker and therefore accumulating enough photons in the spectrometers requires longer acquisition times.

It would be beneficial therefore to have particles that can withstand higher excitation powers and that have a plasmon resonance well defined. In principle gold nanospheres fulfill these requirements. They are known to withstand much higher excitation powers without reshaping nor melting[43]. Moreover the plasmon resonance of spheres shifts only slightly with radius, therefore it is possible to predict it using Mie theory and eliminating the need of a second laser beam. Sphere samples however always show a shape distribution that cannot be neglected and that induces a deviation of the observed resonance from the predicted.

4

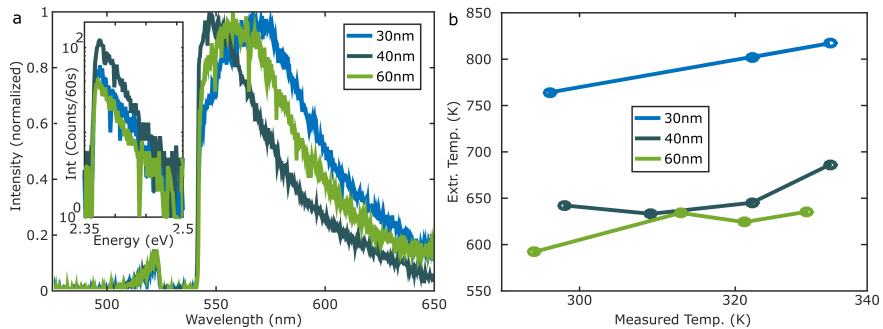


Figure 4.8: Spectra and temperature extraction with spheres of diameter 60 nm, 40 nm and 30 nm. a) Normalized luminescence spectra of three particles under 532 nm excitation. The inset shows the detail of the anti-Stokes emission without normalization. The excitation powers for the three particles were 1.2 mW, 2.0 mW and 3.6 mW respectively. b) Extracted temperature from these particles while increasing the medium temperature.

Figure 4.8.a shows the normalized luminescence spectra of three nanospheres of diameters 60 nm, 40 nm and 30 nm under 532 nm excitation. As for the nanorods, two very distinctive parts of the spectrum are distinguishable, the Stokes at longer wavelengths and the anti-Stokes at shorter ones. From Mie theory it would have been expected a blue shift of the resonance while diminishing the radius of the particles; however the 30 nm one seems to be the more red-shifted. This is most likely due to small anisotropies in the sample, giving rise to slightly different plasmon resonances. The inset in Fig. 4.8.a shows a detail of the anti-Stokes emission for the three spheres without any further normalization. It has to be pointed out, however, that the excitation intensity was 1.2 mW, 2.0 mW and 3.6 mW to compensate for the lower cross sections of the smaller particles.

It has to be noted that spheres have not only a smaller cross section than nanorods of the same volume, but their quantum yield is also one order of magnitude lower than for rods and it holds true for the anti-Stokes emission. This can be compensated by increasing the excitation power up to either reaching a melting temperature of gold or a phase transition of the surrounding liquid that in turn would induce a shift in the plasmon resonance. This is why the powers employed with spheres are much higher than the ones

employed with rods.

Figure 4.8.b shows the extracted temperature of the three particles while increasing the medium temperature. It is possible to see that the small 30 nm diameter sphere is 150 K hotter than both the 40 nm and 60 nm. The three curves show an increasing trend, but in this case the variation of medium temperature amounts to less than 5% the temperature of the particles. The extracted temperature is similar to what would be expected from the heat equation, considering the absorption cross section given by Mie theory. An analysis on the error similar to the one performed with rods yields a relative tolerance of about 5% in the extracted temperature, and therefore is not possible to conclude that the increase in the calculated temperature is in fact given by the increase in the medium temperature.

4.4. CONCLUSIONS

Being able to control and monitor temperature at the nanoscale is of utmost importance in different fields ranging from photothermal therapy[5] to nano fabrication[44]. In this work we have shown a simple procedure that allows to measure the temperature of single gold nanorods and nano spheres while being irradiated under a monochromatic continuous laser. The level of accuracy on the temperature measurement depends on several factors, but for nanorods it can be estimated to be better than 2.5% and for nanospheres around 5%.

The model employed for describing the anti-Stokes emission takes into account the presence of the plasmon, responsible for enhancing the emission as well as Bose-Einstein statistics to explain the distribution of the excited states of the particles. It has been shown that the correct characterization of the plasmonic resonance is fundamental for the proper extraction of temperature, specifically in the cases where the excitation wavelength is red-detuned from the resonance.

Particles with a resonance to the red of the excitation wavelength would be more reliable in the temperature extraction procedure, but would also exhibit a lower emission towards shorter wavelengths. The trade-off between both effects will determine the specific particles that are better suited for each application.

In this work we have also explored the possibility of employing gold nano spheres. Since these particles do not reshape under higher excitation powers it is possible to compensate their lower quantum yield by increasing the irradiation intensity. Moreover samples with a narrow shape distribution would be ideal candidates to temperature extraction since their plasmon can be determined from Mie theory with only one needed parameter, the radius of the particle.

We have observed the anti-Stokes emission from particles with three different diameters. The extracted temperature in each case matches with the expected value from thermal conductivity calculations, but the change when increasing the surrounding medium temperature falls between the experimental error of the procedure.

The main advantage of the proposed method is that it doesn't require any modification or adaptation to existing setups that are capable of recording emission spectra. Moreover there is no need of calibration, since the only free parameter of the model is the absolute temperature of the nanoparticle under study. A 2.5% accuracy in temperature may suffice for several applications. This value can be improved in different

ways: by carefully selecting the particles that show the most favorable plasmon resonance; by determining the plasmon resonance through white-light scattering, avoiding the uncertainty in the parameters; also an ad-hoc calibration of the temperature can be performed.

REFERENCES

- [1] J.-M. Yang, H. Yang, and L. Lin, *Quantum Dot Nano Thermometers Reveal Heterogeneous Local Thermogenesis in Living Cells*, ACS Nano **5**, 5067 (2011).
- [2] C. Hrelescu, J. Stehr, M. Ringler, R. A. Sperling, W. J. Parak, T. A. Klar, and J. Feldmann, *DNA Melting in Gold Nanostove Clusters*, J. Phys. Chem. C **114**, 7401 (2010).
- [3] Y. Li, A. M. Gobin, G. W. Dryden, X. Kang, D. Xiao, S. P. Li, G. Zhang, and R. C. G. Martin, *Infrared light-absorbing gold/gold sulfide nanoparticles induce cell death in esophageal adenocarcinoma*, Int. J. Nanomedicine **8**, 2153 (2013).
- [4] A. M. Gobin, M. H. Lee, N. J. Halas, W. D. James, R. A. Drezek, J. L. West, M. Gobin, M. H. Lee, N. J. Halas, W. D. James, R. A. Drezek, and J. L. West, *Near-Infrared Resonant Nanoshells for Combined Optical Imaging and Photothermal Cancer Therapy*, Nano Lett. **7**, 1929 (2007).
- [5] X. H. Huang, I. H. El-Sayed, W. Qian, and M. a. El-Sayed, *Cancer cell imaging and photothermal therapy in the near-infrared region by using gold nanorods*, J. Am. Chem. Soc. **128**, 2115 (2006).
- [6] S. Huo, S. Jin, X. Ma, X. Xue, K. Yang, A. Kumar, P. C. Wang, J. Zhang, Z. Hu, and X.-J. Liang, *Ultrasmall Gold Nanoparticles as Carriers for Nucleus-Based Gene Therapy Due to Size-Dependent Nuclear Entry*, ACS Nano (2014), 10.1021/nn500857z.
- [7] S. Ebrahimi, Y. Akhlaghi, M. Kompany-Zareh, and A. Rinnan, *Nucleic Acid Based Fluorescent Nanothermometers*, ACS Nano (2014), 10.1021/nn5036944.
- [8] F. Vetrone, R. Naccache, A. Zamarrón, A. Juarranz de la Fuente, F. Sanz-Rodríguez, L. Martínez Maestro, E. Martín Rodriguez, D. Jaque, J. García Solé, and J. A. Capobianco, *Temperature sensing using fluorescent nanothermometers*, ACS Nano **4**, 3254 (2010).
- [9] F. Auzel, *Upconversion and Anti-Stokes Processes with f and d Ions in Solids*, Chem. Rev. **104**, 139 (2004).
- [10] E. A. Pozzi, A. B. Zrimsek, C. M. Lethiec, G. C. Schatz, M. C. Hersam, and R. P. Van Duyne, *Evaluating Single-Molecule Stokes and Anti-Stokes SERS for Nanoscale Thermometry*, J. Phys. Chem. C **119**, 21116 (2015).
- [11] M. Suzuki, V. Zeeb, S. Arai, K. Oyama, and S. Ishiwata, *The 105 gap issue between calculation and measurement in single-cell thermometry*, Nat. Methods **12**, 802 (2015).
- [12] X. Huang, P. K. Jain, I. H. El-Sayed, and M. A. El-Sayed, *Plasmonic photothermal therapy (PPTT) using gold nanoparticles*, Lasers Med. Sci. **23**, 217 (2008).

- [13] L. R. Hirsch, R. J. Stafford, J. a. Bankson, S. R. Sershen, B. Rivera, R. E. Price, J. D. Hazle, N. J. Halas, and J. L. West, *Nanoshell-mediated near-infrared thermal therapy of tumors under magnetic resonance guidance*. Proc. Natl. Acad. Sci. U. S. A. **100**, 13549 (2003), arXiv:0008204 [cond-mat].
- [14] T. Zhao, K. Yu, L. Li, T. Zhang, Z. Guan, N. Gao, P. Yuan, S. Li, S. Q. Yao, Q.-H. Xu, and G. Q. Xu, *Gold Nanorod Enhanced Two-photon Excitation Fluorescence of Photosensitizers for Two-Photon Imaging and Photodynamic Therapy*. ACS Appl. Mater. Interfaces (2014), 10.1021/am405214w.
- [15] J. S. Donner, S. a. Thompson, C. Alonso-Ortega, J. Morales, L. G. Rico, S. I. C. O. Santos, and R. Quidant, *Imaging of plasmonic heating in a living organism*. ACS Nano **7**, 8666 (2013).
- [16] P. Zijlstra and M. Orrit, *Single metal nanoparticles: optical detection, spectroscopy and applications*, Reports Prog. Phys. **74**, 106401 (2011).
- [17] L. Jiang, I. W. Schie, J. Qian, S. He, and T. Huser, *Coherent anti-Stokes emission from gold nanorods and its potential for imaging applications*. Chemphyschem **14**, 1951 (2013).
- [18] M. Hu, C. Novo, A. Funston, H. Wang, H. Staleva, S. Zou, P. Mulvaney, Y. Xia, and G. V. Hartland, *Dark-field microscopy studies of single metal nanoparticles: understanding the factors that influence the linewidth of the localized surface plasmon resonance*, J. Mater. Chem. **18**, 1949 (2008).
- [19] S. Berciaud, D. Lasne, G. Blab, L. Cognet, and B. Lounis, *Photothermal heterodyne imaging of individual metallic nanoparticles: Theory versus experiment*, Phys. Rev. B **73**, 045424 (2006).
- [20] B. Kang, M. M. Afifi, L. a. Austin, and M. a. El-Sayed, *Exploiting the nanoparticle plasmon effect: observing drug delivery dynamics in single cells via Raman/fluorescence imaging spectroscopy*. ACS Nano **7**, 7420 (2013).
- [21] D. P. O'Neal, L. R. Hirsch, N. J. Halas, J. D. Payne, and J. L. West, *Photo-thermal tumor ablation in mice using near infrared-absorbing nanoparticles*, Cancer Lett. **209**, 171 (2004).
- [22] A. Mooradian, *Photoluminescence of metals*, Phys. Rev. Lett. **22**, 185 (1969).
- [23] M. B. Mohamed, V. Volkov, S. Link, and M. A. El-Sayed, *The 'lightning' gold nanorods: fluorescence enhancement of over a million compared to the gold metal*, Chem. Phys. Lett. **317**, 517 (2000).
- [24] M. Beversluis, A. Bouhelier, and L. Novotny, *Continuum generation from single gold nanostructures through near-field mediated intraband transitions*, Phys. Rev. B **68**, 1 (2003).

- [25] Y. Fang, W.-S. Chang, B. Willingham, P. Swanglap, S. Dominguez-Medina, and S. Link, *Plasmon emission quantum yield of single gold nanorods as a function of aspect ratio*, ACS Nano **6**, 7177 (2012).
- [26] W. Rao, Q. Li, Y. Wang, T. Li, and L. Wu, *Comparison of Photoluminescence Quantum Yield of Single Gold Nanobipyramids and Gold Nanorods*, ACS Nano **9**, 2783 (2015).
- [27] M. Yorulmaz, S. Khatua, P. Zijlstra, A. Gaiduk, and M. Orrit, *Luminescence quantum yield of single gold nanorods*, Nano Lett. **12**, 4385 (2012).
- [28] Y. Cheng, G. Lu, Y. He, H. Shen, J. Zhao, K. Xia, and Q. Gong, *Luminescence Quantum Yields of Gold Nanoparticles Varying with Excitation Wavelength*, Nanoscale, 2188 (2015).
- [29] S. Link and M. A. El-Sayed, *Int. Rev. Phys. Chem.*, July (2010) pp. 409–453.
- [30] M. A. Yurkin and A. G. Hoekstra, *The discrete-dipole-approximation code ADDA: Capabilities and known limitations*, J. Quant. Spectrosc. Radiat. Transf. **112**, 2234 (2011).
- [31] E. Dulkeith, T. Niedereichholz, T. a. Klar, J. Feldmann, G. Von Plessen, D. I. Gittins, K. S. Mayya, and F. Caruso, *Plasmon emission in photoexcited gold nanoparticles*, Phys. Rev. B - Condens. Matter Mater. Phys. **70**, 1 (2004).
- [32] J. H. Hodak, A. Henglein, and G. V. Hartland, *Electron-phonon coupling dynamics in very small (between 2 and 8 nm diameter) Au nanoparticles*, J. Chem. Phys. **112**, 5942 (2000).
- [33] A. Giri, J. T. Gaskins, B. M. Foley, R. Cheaito, and P. E. Hopkins, *Experimental evidence of excited electron number density and temperature effects on electron-phonon coupling in gold films*, J. Appl. Phys. **117**, 044305 (2015).
- [34] A. Arbouet, C. Voisin, D. Christofilos, P. Langot, N. D. Fatti, F. Vallée, J. Lermé, G. Celep, E. Cottancin, M. Gaudry, M. Pellarin, M. Broyer, M. Maillard, M. P. Pileni, and M. Treguer, *Electron-Phonon Scattering in Metal Clusters*, Phys. Rev. Lett. **90**, 177401 (2003).
- [35] T. Zhao, J. W. Jarrett, J. S. Johnson, K. Park, R. A. Vaia, and K. L. Knappenberger, *Plasmon Dephasing in Gold Nanorods Studied Using Single-Nanoparticle Interferometric Nonlinear Optical Microscopy*, J. Phys. Chem. C **120**, 4071 (2016).
- [36] C. Sönnichsen, T. Franzl, T. Wilk, G. von Plessen, J. Feldmann, O. Wilson, and P. Mulvaney, *Drastic reduction of plasmon damping in gold nanorods*, Phys. Rev. Lett. **88**, 077402 (2002).
- [37] C. K. Sun, F. Vallée, L. H. Acioli, E. P. Ippen, and J. G. Fujimoto, *Femtosecond-tunable measurement of electron thermalization in gold*, Phys. Rev. B **50**, 15337 (1994).
- [38] V. K. Pustovalov, *Theoretical study of heating of spherical nanoparticle in media by short laser pulses*, Chem. Phys. **308**, 103 (2005).

- [39] G. Baffou, P. Berto, E. Bermúdez Ureña, R. Quidant, S. Monneret, J. Polleux, and H. Rigneault, *Photoinduced Heating of Nanoparticle Arrays*. ACS Nano (2013), 10.1021/nn401924n.
- [40] Y. He, K. Xia, G. Lu, H. Shen, Y. Cheng, Y.-c. Liu, K. Shi, Y.-F. Xiao, and Q. Gong, *Surface enhanced anti-Stokes one-photon luminescence from single gold nanorods*, Nanoscale **7**, 577 (2015).
- [41] G. T. Boyd, Z. H. Yu, and Y. R. Shen, *Photoinduced luminescence from the noble metals and its enhancement on roughened surfaces*, Phys. Rev. B **33**, 7923 (1986).
- [42] A. Konrad, F. Wackenhut, M. Hussels, A. J. Meixner, and M. Brecht, *Temperature Dependent Luminescence and Dephasing of Gold Nanorods*, J. Phys. Chem. C **117**, 21476 (2013).
- [43] L. Hou, M. Yorulmaz, N. R. Verhart, and M. Orrit, *Explosive formation and dynamics of vapor nanobubbles around a continuously heated gold nanosphere*, New J. Phys. **17**, 13050 (2015).
- [44] M. Fedoruk, M. Meixner, S. Carretero-Palacios, T. Lohmüller, and J. Feldmann, *Nanolithography by Plasmonic Heating and Optical Manipulation of Gold Nanoparticles*. ACS Nano (2013), 10.1021/nn402124p.



A

SUPPLEMENTARY INFORMATION FOR: *In situ* TUNING OF GOLD NANOROD PLASMON THROUGH OXIDATIVE CYANIDE ETCHING

A.1. SOLUTION RESULTS

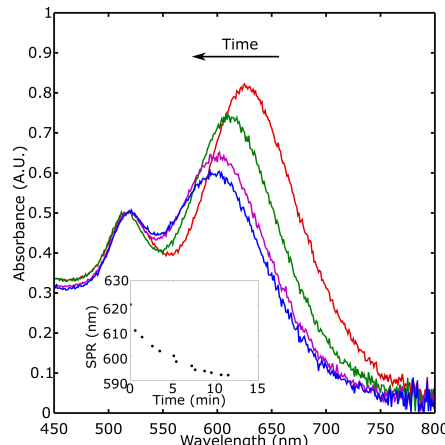


Figure A.1: Extinction spectra of a bulk suspension of gold nanorods dispersed in $100\mu\text{M}$ KCN. The curves are displayed at 2 minutes intervals. The inset shows the peak position as a function of time. The curves were normalized to the transverse peak for clarity.

Figure SA.1 shows the behavior of nanorods dispersed in $100\mu\text{M}$ KCN. The same sample than for the single-particle experiments was used. We observe a clear blue shift

A

of the longitudinal plasmon resonance, towards the transverse peak at around 530 nm. As stated in the main text, we attribute the blue shift of the peak to a shortening of the long axis of the rods. This is because the CTAB is more efficient in protecting the sides than the tips of the particles. The blue shift does not seem stabilized for the last spectrum. We attribute this to a complete consumption of KCN by excess gold metal in our sample. If more KCN had been added, the blue-shift would probably have continued.

The spectra were acquired in an UV-Vis spectrometer. The first spectrum was acquired with the rods dispersed in water, before adding KCN into the cuvette. Later a solution such that the final concentration was $100 \mu\text{M}$ was added and a set of automatic spectra was recorded at a fixed interval of time. The peak position was extracted by fitting a double Lorentzian, one with a fixed central wavelength (the transverse resonance) and a second one for the longitudinal plasmon.

A.2. SEM IMAGES

Samples for SEM images were prepared by drop casting a suspension of gold nanorods into clean silicon wafers. An initial image of several hundreds of rods was acquired before any etching. The same samples were placed in a solution of KCN for 2 minutes and imaged again. Finally they were submersed again for 2 minutes in KCN and imaged afterwards. In this way, even if it was not possible to track the same particles during the etching process, it was possible to reproduce the conditions in which the reshaping took place on the optical microscope.

Figure SA.2 shows the SEM images of the rods. In SA.2a,b an example of the rods after synthesis and before etching at two different magnifications. Figures SA.2c and d show the rods after 2 minutes and 4 minutes in $20 \mu\text{M}$ KCN. Figure SA.2e was acquired after 4 minutes in KCN; the difference on the shape of the particles when they are in contact is notable. It has to be reminded however that the clusters of rods were already formed on the substrate before the etching started. Drop casting a suspension of rods tends to form conglomerates of particles rather than isolated particles as can be easily achieved by spin casting and shown in the optical experiments in the main text.

Histograms in Figures SA.2f-h show the analysis of the aspect ratio, the longitudinal and the transverse axes respectively for each of the cases. Table 1 summarizes the average values found after analyzing approximately 300 particles. The shift is rather small as compared to the standard deviation of the distribution of sizes.

	L (nm)	Sdv (nm)	D (nm)	Sdv (nm)
0min	51	5	24	3
2min	50	5	23	3
4min	49	5	22	2

Table A.1: Summary of the results obtained for 300 different particles while imaging them with an SEM. L and D are the length and diameter respectively. Sdv is the standard deviation of the values

A

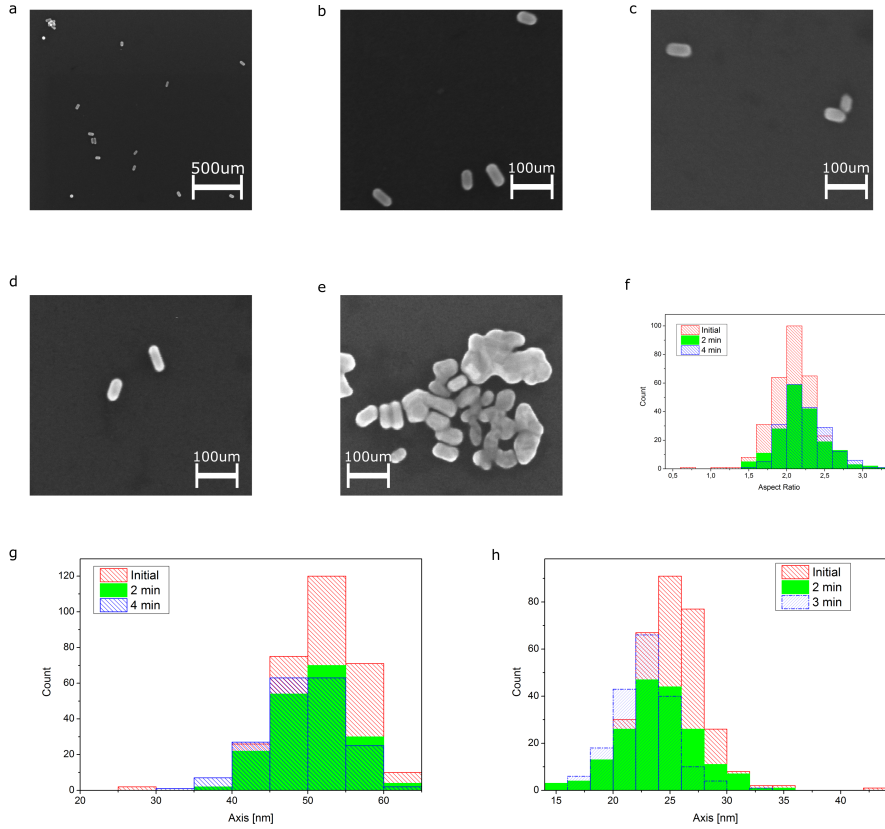


Figure A.2: SEM images of the rods a-b) after synthesis, at different magnifications c) after 2 minutes in 20 μM KCN. d) after 4 minutes in KCN and e) when they were forming clusters. f-h) Histograms of the aspect ratio (f), longitudinal(g) and transverse axis(h) before, after 2 and after 4 minutes in KCN. The distribution of values is too broad to visualize a shift in aspect ratio. Statistics on the values, however, show a slight increase and the data is summarized in table 1.

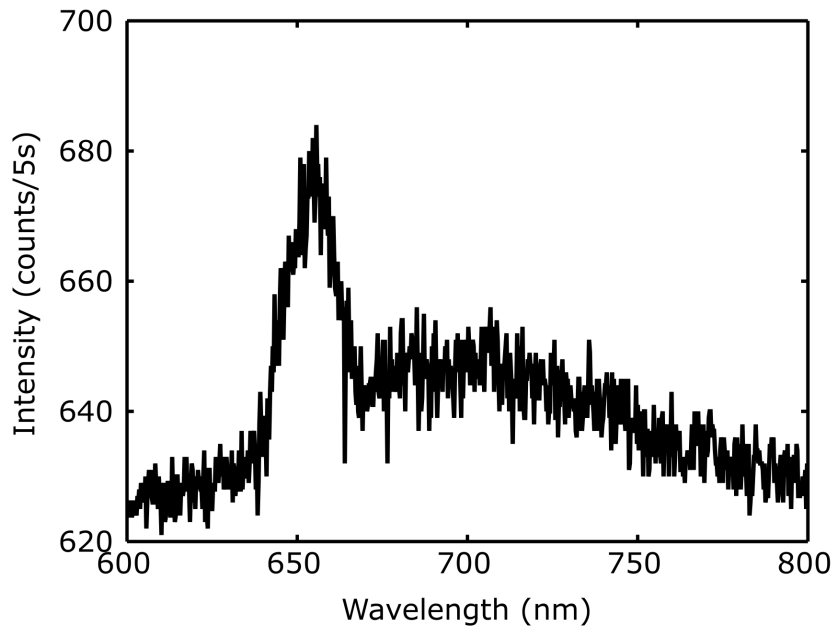


Figure A.3: Spectra from the background while exciting with a 532 nm laser. The peak appearing at 650 nm is attributed to Raman scattering from the O-H stretching modes of water.

A.3. BACKGROUND SPECTRUM

Figure SA.3 shows the typical background when exciting with a 532nm laser. The peak at 650nm is attributed to Raman scattering from water. Normally this background can be well subtracted from the spectra acquired on particles. For less intense curves however, it is possible to observe a shoulder appearing at this particular wavelength. This indicates a non-additive phenomenon that we attributed to enhanced Raman scattering close to the nanoparticles.



B

BACKGROUND-FREE IMAGING OF GOLD NANORODS THROUGH DETECTION OF ANTI-STOKES EMISSION

B.1. SETUP

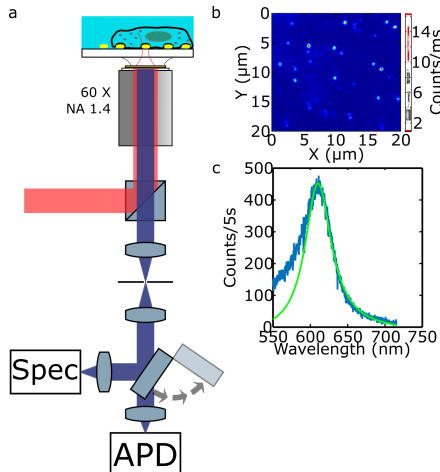


Figure B.1: Experimental setup and examples of observations. a) Simplified schematic of the confocal microscope employed during the measurements. b) A typical 1-photon luminescence raster scan of the sample immersed in water c) luminescence spectrum of a single rod.

Figure B.1 shows the schematic of the confocal microscope employed in the experi-

B

ments. It is important to note the presence of a 50/50 beamsplitter before the objective. Exchanging it for an appropriate dichroic mirror would increase the collection efficiency. In this work we chose not to do it because the beamsplitter allows to collect both the full emission under 532 nm excitation and the Stokes/anti-Stokes emission under 633 nm without changes in the optical path.

B.2. UV-VIS SPECTRUM

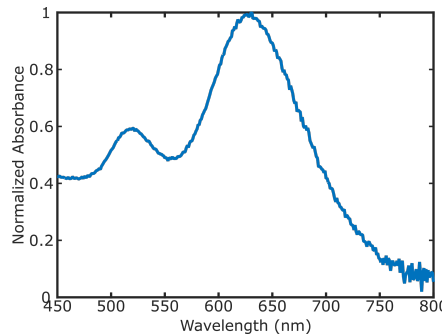


Figure B.2: Normalized extinction spectrum of a suspension of nanorods after synthesis. The resonance maximum is located at 630 nm.

Figure B.2 shows the extinction spectrum of the nanorod samples used throughout this work. Two peaks are clearly distinguishable, one around 630 nm that corresponds to the longitudinal plasmon resonance (LPR) of particles with sizes 50 nm × 23 nm and a second one at around 520 nm. This peak also includes contributions of spheres as by-products of the synthesis of the rods. The transverse plasmon resonance is also located at the same wavelength but is much weaker than the LPR. In a sample consisting exclusively of rods, the transverse resonance would be barely observable in a UV-Vis spectrometer.

B.3. FILTERS

The selection of filters plays a crucial role in the signal acquired. Since the main part of the anti-Stokes emission is concentrated around the excitation wavelength, it is important to select filters that have a high transmission close to the laser line. Figure B.3 shows the normalized absorption spectrum of two notch filters and a short pass. Both notch filters are branded as NF03 – 633E – 25 but show a slightly different absorption spectrum, shifted roughly 4 nm from each other. The shortpass filter (branded as SP01 – 633RU – 25) shows the transition to transmission even closer to the laser line.

For many fluorescence applications the exact shape of the transmission spectrum of the filters does not play a crucial role. However for anti-Stokes imaging, since the shape of the emission is exponential-like, minute changes in the transmission spectrum can have a great impact on the signal collected. For example, changing from a detection path with a spectrum like notch 1 to one like shortpass (i.e. shifting in about 7 nm the edge of the filter) increases the collected number of photons by about 50%.

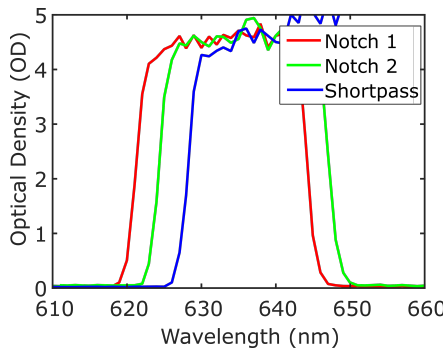


Figure B.3: Transmission spectrum of two notch filters and a short pass filter (Semrock).

In this work, since only one filter does not provide enough attenuation, care was taken to always employ the notch with the most favorable transmission spectrum in combination with either a shortpass or a longpass filter. Ideally, two shortpass filters would have been the best solution.

B.4. TEM IMAGES OF RODS

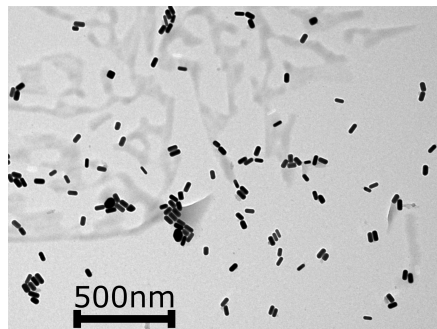


Figure B.4: TEM image of the nanorod sample. The scale bar is 500 μm .

Figure B.4 shows an example TEM image of the gold nanorod sample. Analysis on the dimensions of the particles yield an average length of 50 nm and diameter of 23 nm. This is consistent with the plasmon observed in fig. B.2 and at a single-particle level as in fig. B.1c.

B.5. WHITE LIGHT TRANSMISSION

B.6. FULL SCAN WITHOUT DYE

The raster scan shown in Figure B.6 corresponds to a larger area comprising the same region shown in the main text. The majority of the particles has a much larger contrast in the anti-Stokes. Moreover it can be noted that the background is flat. In the Stokes

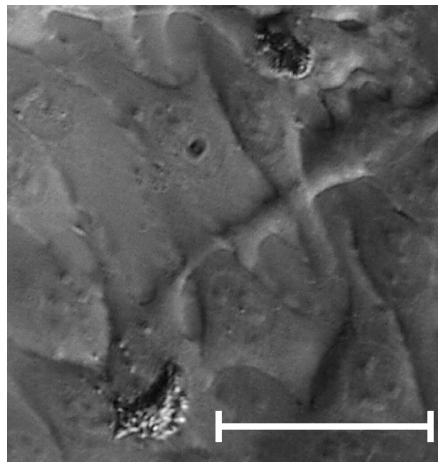


Figure B.5: White light transmission image of the sample with cells deposited on top of the rods. It is possible to observe that they cover entirely the observed region without spacing in between them. The scale bar in the figure is $20\mu\text{m}$ in length.

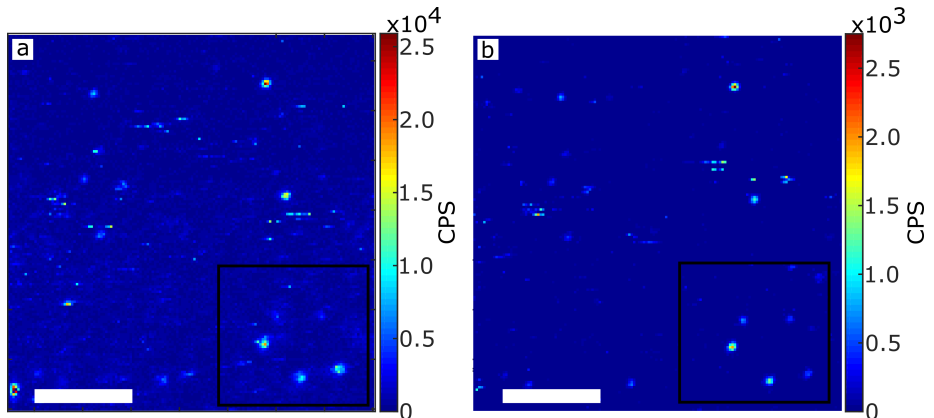


Figure B.6: Raster scan of a nanorod sample under HeLa cells using (a) a long pass filter and (b) a short pass filter for photoluminescence detection. Both scans contain the same region shown in the main text and here marked with a black square. The scale bar in both figures is $4\mu\text{m}$ in length.

image the nanorods are still visible, but the contrast is obviously lower.

B.7. FULL SCAN WITHOUT DYE

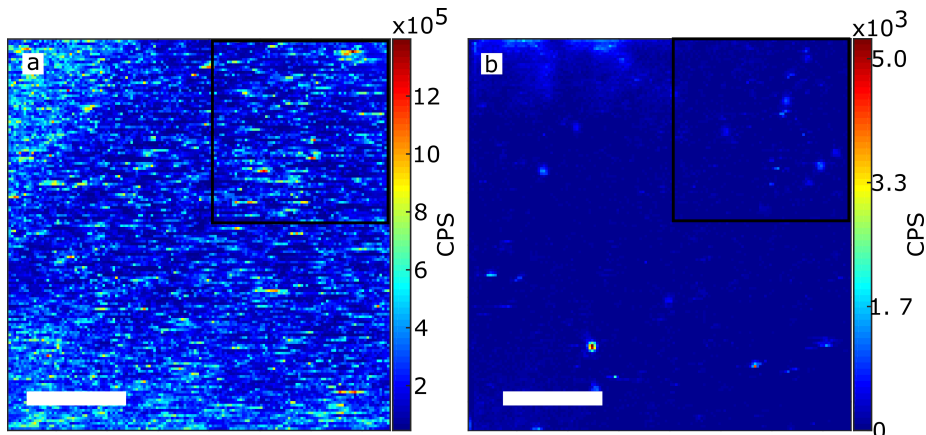


Figure B.7: Raster scan of a nanorod sample under stained HeLa cells using (a) a long pass filter and (b) a short pass filter for photoluminescence detection. Both scans contain the same region shown in the main text and here marked with a black square. The scale bar in both figures is $4\mu\text{m}$ in length.

Figure B.7 shows a raster scan of gold nanorods under cells stained with ATTO 647N. Both images comprise the same region shown in the main text, here marked with a black square. No particles can be detected in the Stokes image, while several nanorods are visible in the anti-Stokes image with a high signal-to-background. We note, however, that there is some background appearing in the top left part of the anti-Stokes image. This may be due to an increase of the concentration of ATTO 647N. The incubation procedure does not prevent the accumulation of dye in specific organelles of the cells, and there is no control on the final dye concentration.